# Calibrations of the Hubble Space Telescope Optical Telescope Assembly

H. Hasan[1] and C. J. Burrows[1,2]

**Abstract**

Three major calibrations of the Hubble Space Telescope Optical Telescope Assembly (OTA) are described in this paper. They are: (1) the OTA focus, which includes the definition of the best focus, long term focus changes caused by desorption of the OTA metering truss, secondary mirror moves made to correct desorption related focus changes and thermally driven short term focus variations; (2) the Telescope Image Modelling (TIM) software, which can be used to simulate point spread functions and star fields; (3) measurements of light scattering caused by microroughness in the OTA primary mirror.

## I. Introduction

The Optical Telescope Assembly of the Hubble Space Telescope (*HST*) is a 2.4 m hyperbolic primary mirror and a 31 cm secondary mirror, both mounted on a graphite epoxy metering truss. The original Ritchey-Chrétien system was designed to produce diffraction limited images. However, the primary mirror manufactured was defective, leading to images blurred by spherical aberration (Burrows et al., 1991). As a result, no position of the secondary mirror gives optimal imaging simultaneously for all wavelengths and for all science instruments aboard *HST*. In the first part of this paper (section II) we trace the focus history of *HST* from launch till November 1993. In section III we outline the Telescope Image Modelling (TIM) software which was developed to simulate images of point sources on a pixellated detector, and which is available to the scientific community for computing point spread functions. Finally, in section IV we summarize the results of an observatory level test performed to measure the microroughness scattering from the OTA primary mirror.

## II. Focus History

### Introduction

Soon after discovery of spherical aberration in the *HST* primary mirror a sub-committee of the Science Working Group (SWG) was assigned the task of defining a position of best focus for the OTA which would be acceptable for all science instruments aboard *HST*. The definition adopted by the SWG was that the best focus was that position of the OTA secondary mirror which gave maximum encircled energy at 486 nm within a 0.1 arcsec radius in a stellar image taken with the Faint

1. Space Telescope Science Institute, Baltimore, MD 21218
2. Affiliated to the Space Science Department of ESA.

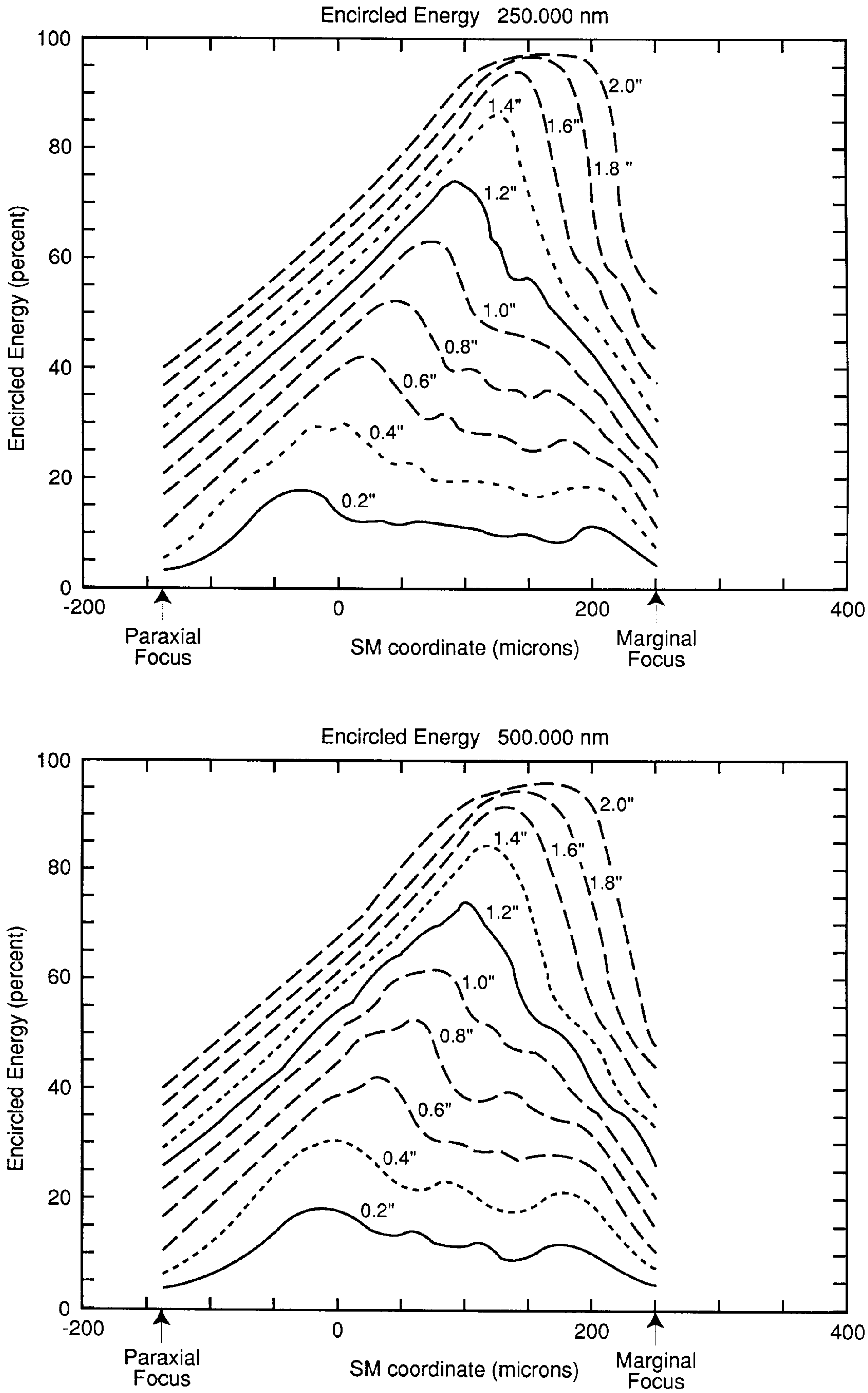


Figure 1: Encircled energies through apertures with diameters varying from 0.2 arcsec to 2 arcsec, versus focus position at (a) 250 nm and (b) 500 nm. The zero of the SM coordinate scale corresponds to the adopted focus with negative values corresponding to SM positions closer to the primary .

Object Camera (FOC) in the *f*/96 mode. The focus position thus defined is a compromise for the cameras and the spectrographs as is apparent by examining results from simulations plotted in Figure 1. The encircled energy (EE) within apertures of radii varying from 0.1 arcsec to 1 arcsec are plotted as a function of secondary mirror position for two different wavelengths. The first point to note is that for both wavelengths, the peak in the EE curves moves towards greater separations of the primary and secondary mirrors as the aperture size is increased, indicating that while the adopted best focus gives close to maximum throughput for the small apertures in the spectrographs, for the large apertures a *greater* mirror separation would be preferable. Secondly, in the UV the peak EE is obtained for mirror separations *smaller* than the adopted best focus. The cameras, which are used primarily for imaging in the visible would give optimal results at the adopted best focus.

In April 1991, the Project appointed a panel of optical experts, the Optical Alignment Panel (OAP) to examine the alignment of the OTA and the science instruments, and assess the focus position of the telescope. Based on the results of tests, the OAP concluded that the collimation of the OTA secondary mirror on October 18, 1991 had a 1/15th wave of coma at 633 nm and that it was 5 microns closer to the primary mirror than desired (Schroeder, 1991). However, since considerable calibration data had been obtained at that position, a decision was taken not to recollimate the telescope and to maintain the October 18, 1991 focus position till the refurbishment mission scheduled for December 1993.

## Focus monitoring

The focus of the OTA is expected to change with time, because the graphite epoxy metering truss desorbs water and so shrinks, reducing the distance between the primary and secondary mirrors. The secondary mirror, therefore, has to be moved back to compensate for the desorption. In order to monitor the OTA desorption and focus, a test was designed and has been executed regularly since August 1990. The test consists of taking four 15 min. exposures of a standard star with the FOC *f*/96 through the filter F486N. The images are co-added and analyzed to obtain the secondary mirror position. In addition to this test, since May 1992, monthly stellar monitoring images from the Wide Field and Planetary Cameras (WFPC) have also been analyzed to provide trending information. The WFPC images are of poor quality for purposes of accurate focus monitoring but are adequate for trending purposes. Two methods have been used for the analysis: pad method and phase retrieval (Hasan et al., 1993).

*Pad Method*. This method exploits the fact that the three pads supporting the OTA primary mirror are clearly visible in well-exposed stellar images. By measuring the radial distances of the pads from the image center, the distance $\Delta(SM)$ of the secondary mirror from its nominal position that places the focal plane at paraxial focus, is obtained by ray trace from the relation,

$$\langle r \rangle \ (microns) = 596.5 - 1.998\Delta(SM) \ (microns) , \qquad (1)$$

where < $r$ > is the mean radial distance of the pads.

*Phase retrieval method*. In this method a simulated image is fitted to the data and a merit function minimized. The fit parameters correspond to aberration coefficients used to construct the simulated point spread function (PSF). The best fit parameters give the aberration coefficients which can be used to estimate the secondary mirror position.

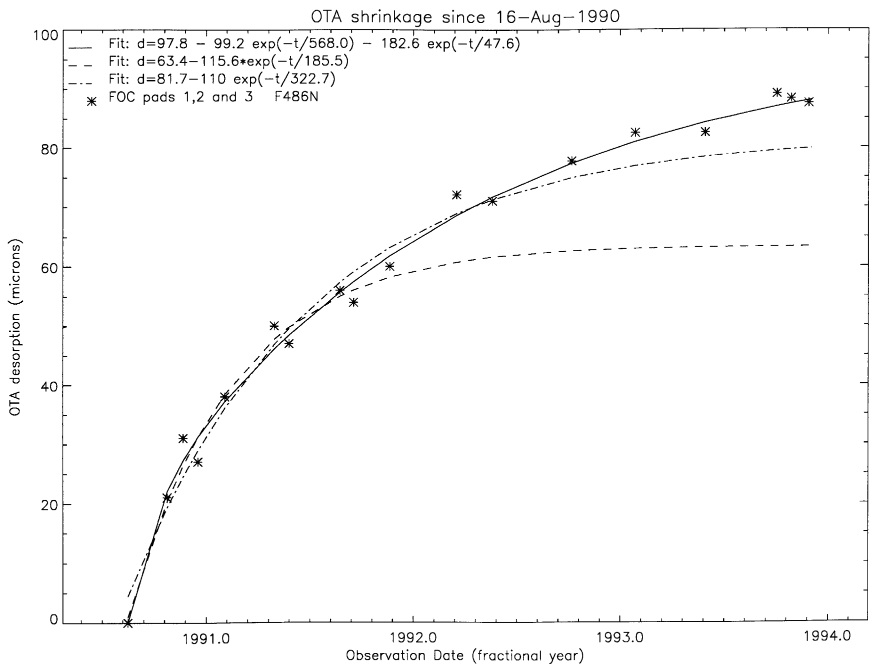


Figure 2: Best-fit curves for FOC desorption data available until 1991 November 20 (dashed curve), 1992 May 19 (dot-dash curve) and current best fit.

## Results

OTA desorption measured from August 1990 through November 1991 was fitted with the exponential curve shown by a dashed line in Figure 2. The data from March 1992 showed a big departure from this curve and the May 1992 data confirmed March results. Another exponential curve was fitted (dot-dashed line). The data from October 1992 and January 1993 did not follow predictions. The data from August 1990 through January 1993 was re-fitted with a double exponential (solid line), which suggests that different parts of the OTA are perhaps desorbing at different rates. The subsequent data through November 1993 follow the new curve.

The FOC data are re-plotted with the PC stellar monitoring data in Figure 3, together with the mirror moves made to counter desorption. The move in November 1993 was an overcorrection by 5 microns, with the philosophy that the focus will be maintained within 5 microns of the October 18, 1991 position. The November 1993 move was the last correction made prior to the first servicing mission.

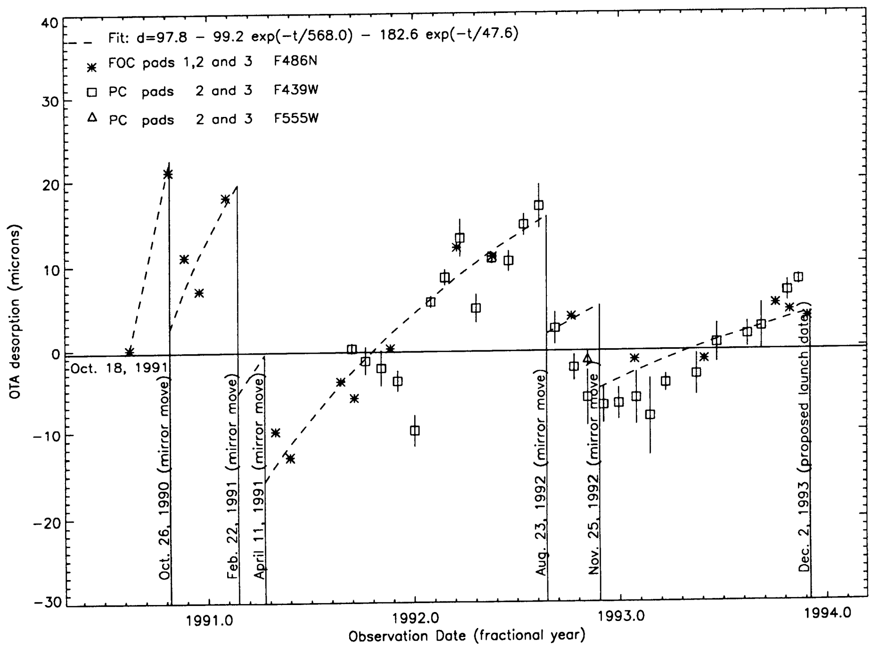


Figure 3: OTA desorption measured from FOC and PC data overplotted with the best fit curve (dashed line) is shown together with mirror moves. The adopted focus (October 18, 1991 focus position) is shown as a solid, while breaks in the dashed curve indicate the mirror moves.

## OTA Breathing

Short term focus variations of the order of 2 – 5 microns over an orbital period, seen in FOC and PC images are referred to as OTA breathing. Such focus variations cannot be attributed to OTA desorption. Tests were run to characterize the breathing, in December 1992 and May 1993. In the December 1992 test, 34 PC images were taken of a star in the continuous viewing zone (CVZ) over six orbital periods. Focus variations corresponding to secondary mirror movements of ~ 0.2 – 5 microns were observed. In the May 1993 test, two targets – one in the CVZ and the other in the ecliptic plane – were viewed both with the FOC and PC. Again, focus variations of the same order as before were obtained. Similar focus variations have also been measured in images taken for the desorption test. The cause of these variations is under investigation, though there is a strong indication that they are thermally induced.

In addition to the short term focus variations, a long term trend is obtained by plotting departures from the best fit curve of the FOC desorption monitoring data and the WFPC stellar monitoring data (Figure 4). While most of the departures fall within ± 5 microns, there are a few cases where secondary mirror movements of 8 – 15 microns have been observed.

Simulations show that focus variations caused by secondary mirror movements of ~ 5 microns will not be detrimental to the refurbished instruments (Hasan and Bely, 1994) in the visible, though there will be a greater impact in the UV. Larger variations appear to be relatively infrequent and may be related to *HST* pointing.

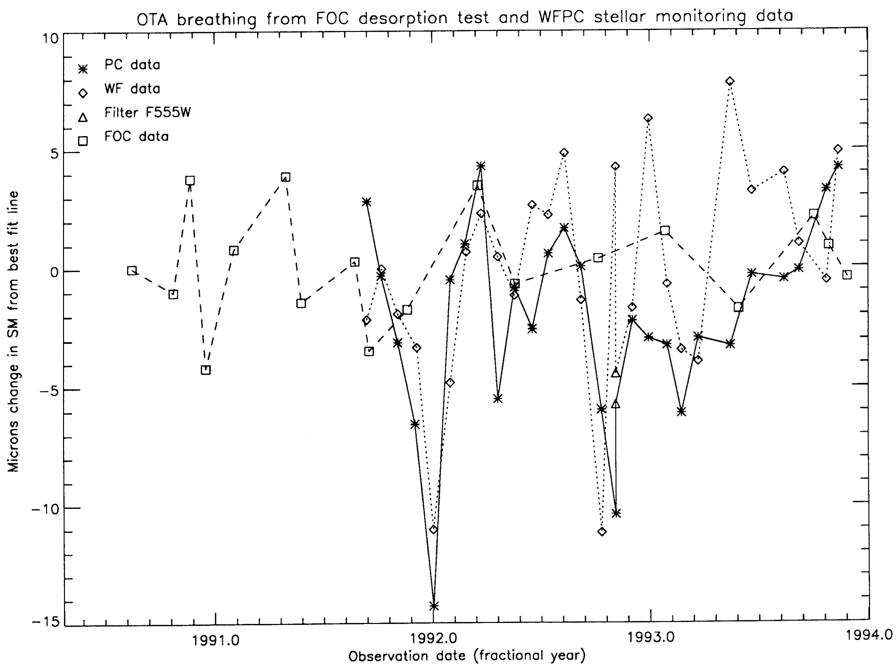


Figure 4: A measure of OTA breathing shown as departures of the FOC desorption data and WFPC stellar monitoring data from the best fit curve.

## III. Telescope Image Modelling (TIM)

The Telescope Image Modelling (TIM) software was developed at STScI primarily for modelling the PSF and images obtained from the science instruments aboard *HST*. However, it is general enough for wider applications. The software has many uses some of which are listed below.

- Study of characteristics of the PSF, such as the effect of different aberrations.
- Analysis of *HST* images.
- Estimation of observation time in planning observations.
- Simulating PSFs for deconvolution.
- Estimating aperture throughput in the spectrographs.

Several issues have to be addressed when simulating PSFs. Some important ones for *HST* which have been modelled in TIM are the effect on the PSF of

- Focus position of the OTA secondary mirror. (TIM contains data on all moves made to counter desorption, and the desorption model described in section 2.)
- Details of primary and secondary mirror smoothness which cause low order aberrations as well as scattering at large angles (section 4.)

- For the WFPC, field dependence caused by the obscuration of the light beam by the secondary mirror of the repeators.
- Internal optics of the cameras which may introduce other aberrations such as spherical and coma.
- Spacecraft jitter which tends to blur the PSF.

**Program stages and outputs**

The program runs in five stages and may be run up to any stage that the user desires. At the ends of each stage some outputs become available. The five stages and outputs are summarized as follows.

*Stage I*. The **amplitude function (ASF)** is computed based on user defined aberrations in the form of Zernike polynomial coefficients and a description of pupil obscurations. An option is available to include low order aberrations caused by imperfections in the primary and secondary mirror, provided in the form of maps by Hughes Danbury. A wavefront error map is also generated.

*Stage II*. A **critically sampled PSF** is generated as the Fourier transform of the ASF. At this stage effects of mirror microroughness scattering, dust, jitter, and even seeing may be included if desired. Several output options are available.

*Stage III*. The above PSF may be **resampled** or **integrated** on user defined pixels. Encircled/ensquared energies are also computed. As in stage II, several output options are available.

*Stage IV*. A **polychromatic PSF** or a **star field** may be simulated at this stage. Throughputs for all *HST* filters are available.

*Stage V*. At this stage **detector defects** such as background, bias, dark current, cosmic rays etc. may be added to the image generated in stage IV.

**Availability of TIM**

TIM is available to the scientific community. It may be retrieved from the Space Telescope Information System (STEIS) or a tape may be obtained from the User Support Branch at STScI.

## IV. Microroughness scattering from *HST* primary mirror

The effect on the PSF of large angle light scattering caused by imperfections on the surface of the *HST* primary mirror were examined by means of an observatory level test (Hasan and Burrows, 1993). A bright star, HD95418($\beta$UMa), $V = 2.35$ was imaged with the Wide Field Camera through three different filters — F889N, F487N and F284W. For each filter, three sets of observations were taken. The star was first centered in chip W1 and imaged with the filter in combination with the neutral density filter, F8ND, so that an unsaturated image of the star was obtained. In the following two exposures, the star was placed in chip W2, 2.5 arcsec and 6 arcsec respectively from the edge of chip W1. The exposure times were so chosen that the images in chip W1 were not saturated. By combining images in chip W1, from the three exposures, a PSF out to 75 arcsec was obtained.

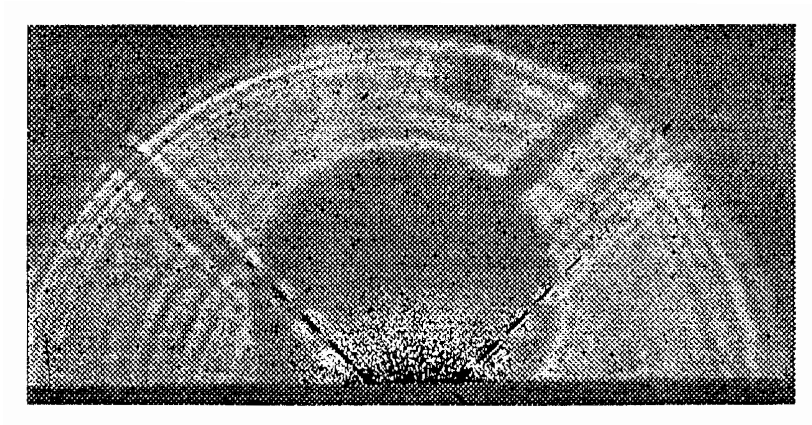

Figure 5: Star image at the edge of chip W1 surrounded by circular ghost caused by reflection off the CCD followed by reflection off the filter.

The star image in chip W1 in the second and third set of exposures was surrounded by a circular shadow caused by obscuration of the beam by the WFC relay secondary mirror. The region outside this shadow had a circular bright ghost similar to that seen in other WFC images of bright stars (Figure 5). The ghost is caused by reflection off the CCD followed by reflection off the filter (this problem has been corrected in the PC camera of WFPC2 by tilting the chip by a small angle). The presence of the ghost limits the extent of determination of the PSF. However, data in the shadow region is sufficient to give us an adequate PSF. Another feature observed in the images is the presence of light in dead pixels, which lie in the pyramid shadow. Some of the light is due to diffraction off the pyramid edge.

## Analysis of data

The raw data was first treated for removal of cosmic rays and bias. It was then flat fielded and a dark current and background subtracted. Finally, an azimuthally averaged normalized PSF was extracted. For the first set of exposures this was done by averaging contributions to the PSF at different radial points from the star center to ~ 1.5 arcsec. The PSF was normalized with the total number of counts within a box size (200 $\times$ 200) centered on the PSF. Star centers for the second and third set of images were obtained by estimating the intersection of the spider diffraction spikes in the images in chips W1 and W2. The radial profile was obtained by averaging contributions to the PSF at different radial points from a wedge in the star image in W2. The wedge was centered at the star center and its angle appropriately chosen so that images of the spiders visible in the ghost surrounding the image were not included. The normalized radial profiles from the three observation sets were overplotted to give the azimuthally averaged PSF for further analysis. The radial profile for filter F284W is shown in Figure 6.

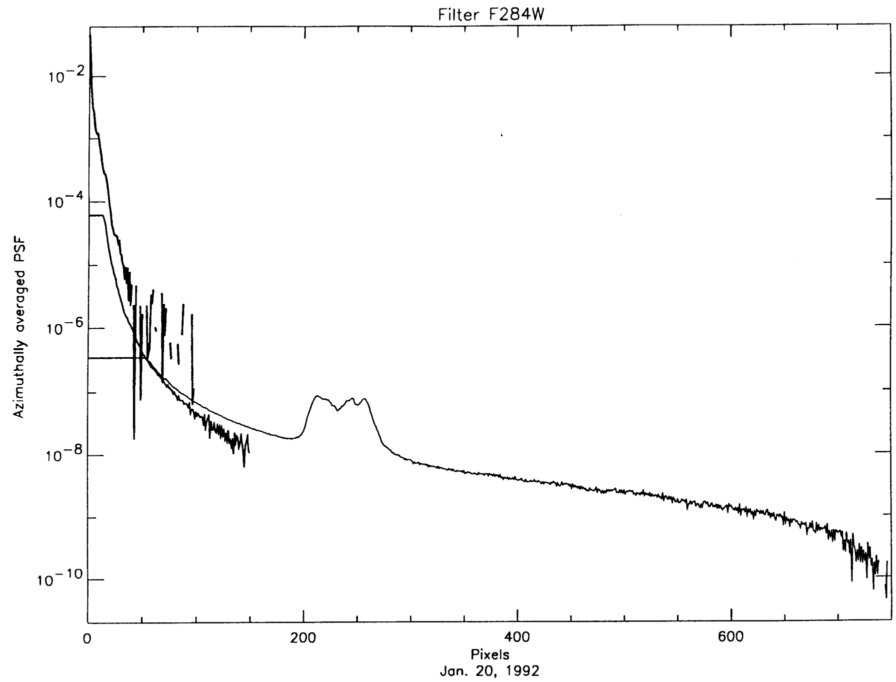


Figure 6: Azimuthally averaged PSF for filter F284W . The bump at ~ 250 pixels corresponds to the ghost seen in the image.

**Results**

*Theoretical Model* . Light scattered by microroughness in the primary mirror will manifest itself primarily in the wings of the PSF , where an increase in intensity will be observed. The effect is modelled by fitting a power law to the measured power spectrum (Brown and Burrows, 1990). The power spectral density , $G(K)$, for the mirror microstructure surface errors (not wavefront errors) is expressed as

$$G(K) = \alpha K^{-\beta} \tag{2}$$

where $\beta$ is the power law exponent, $\alpha$ is related to the RMS microroughness $\delta_e^2$ and $K = 2\pi\theta/\lambda$ for angle $\theta$ and light of wavelength $\lambda$. The total integrated scattering ( *TIS* ) is then given by

$$TIS = \frac{8\pi\alpha}{\lambda^2(\beta-2)} \frac{2\pi}{d_{lim}^{2-\beta}} \tag{3}$$

where $d_{lim} = \lambda/\theta_{min}$ corresponds to the smallest scattering angle $\theta_{min}$ used in the simulation. The new PSF is given by

$$(PSF)_{new} = (1 - TIS)\,PSF_0 + \left|\frac{16\pi^2}{\lambda^4}G(K)\right|_{\theta > \theta_{min}} \qquad (4)$$

where $PSF_0$ is the PSF without scattering effects. A good fit to the metrology data is obtained for $G(K)$ with $\alpha = 6321$, $\beta = 2.16$ for the wave number $K$ in cm$^{-1}$ and $G(K)$ in microns$^4$. This gives a value $\delta_e = 0.0132$ waves at 633 nm in the bandpass $K_1 > 0.5$ cm$^{-1}$ or, $d < 120$ mm, corresponding to scattering angles beyond the 20th Airy ring. The metrology data give no indication of the power spectrum in their bandpass, only the total power. Therefore the details of the scattering beyond the 1000th ring or so are very uncertain.

The model is well behaved at large angles. However, within the first 20 Airy rings, the fit to the power spectrum breaks down. Since the purpose of the scattering test is to study the effects of scattering on the PSF at large angles, this theory is adequate for the present purpose.

*Comparison with data*. The observed azimuthally averaged profiles are compared with PSFs simulated using TIM (section 3). The results are plotted in Figure 7. It can be seen from the plots that for all three filters the intensity of the observed PSF falls off faster than the pre-launch predictions. At 889 nm there is little contribution from scattering caused by microroughness in the mirror, while at 487 nm and 284 m, the microroughness scattering is smaller than predictions. The values of the parameters $\delta_e$ and $\beta$ in the theoretical model were adjusted to approximately fit the data by eye for the F284W filter in the region between 40 and 150 pixels. The data in the region beyond about 120 pixels is higher than the fitted curve because there is a contribution from the ghost visible in the image (the ghost appears as a bump in the azimuthally averaged profile). As we go further into the tail region we get contributions from other fainter ghosts not visible in this image but expected to be there because of multiple reflections of the pupil and ghost images. The values of $\delta_e$ and $\beta$ that fit the data are 0.0096 for $K_1 > 0.5$ cm$^{-1}$ and 2.5 respectively. These values have been used to compute the fitted curves shown in Figures 7a–c.

## References

Brown, R. A. and Burrows, C. J. 1990, Icarus, 87, 484

Burrows, C. J., Holtzman, J. A., Faber, S. M., Bely, P. Y., Hasan, H., Lynds, C. R. and Schroeder, D. 1991, ApJ, 369, L21

Hasan, H. and Bely, P. Y. 1994, in The Restoration of *HST* Images and Spectra II, ed. R. J. Hanisch and R. L. White (in press)

Hasan, H., Burrows, C. J. and Schroeder, D. J. 1993, PASP, 105, 1 184

Hasan, H. and Burrows, C. J. 1993, in Space Astronomical Telescopes and Instrumentation II ed. P. Y. Bely and J. B. Breckinridge (Bellingham:SPIE)36.

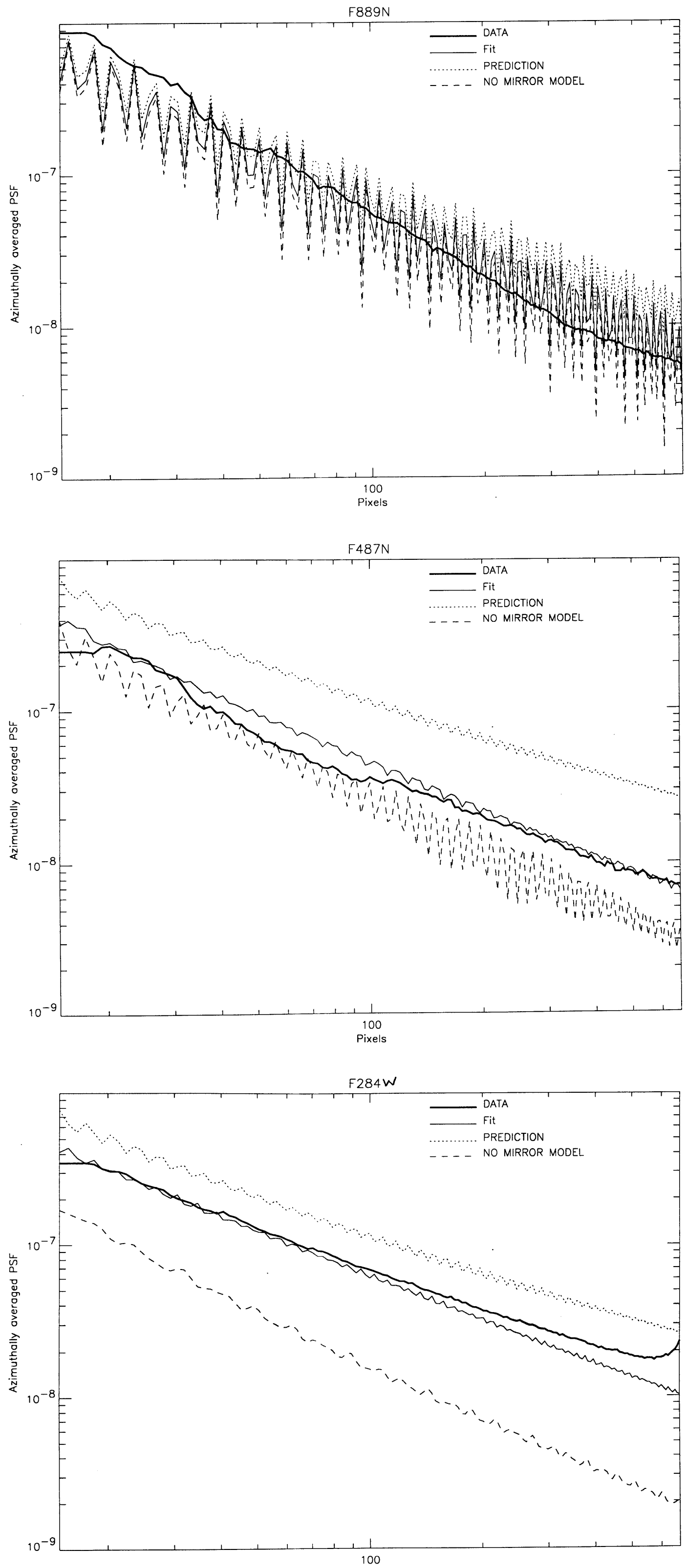


a.

b.

c.

Figure 7: Azimuthally averaged PSF obtained from observations overplotted with simulated PSFs for filters (a) F889N (b) F487N and (c) F284W . The measured PSFs show less large angle scattering caused by mirror microroughness than predicted.

## The UV Sky Background

Adeline Caulet [1,2]

### Summary

The sky background viewed from a space observatory is much darker than from the ground at all wavelengths. At the altitude of *HST* of 600 km, the main sources of the sky background include: variable airglow emission lines arising in the upper atmosphere from Lyman alpha at 1216Å, and OI emission at 1304 and 1356Å; the diffuse galactic light (DGL) below 2500Å from galactic starlight scattered by dust grains in the interstellar medium; and longward of 2500Å, the zodiacal light from the scattering of sunlight in the plane of the ecliptic. Here we present the results of a novel method of measuring the dominant components of the sky brightness from the *HST* orbit. We have used 50 FUVOP objective prism spectra taken with the Faint Object Camera between November 1990 and August 1991.

Typical exposure times were around 900 seconds. The 0.8 arcsec FOC finger occults the field of the f/96 camera, projecting a shadow against the background light of the sky. When the field is dispersed with the objective prism, there are three shadow features in the image corresponding to the dominant sky background components, the geocoronal Lyα and OI airglow emission lines and the zodiacal light continuum. The DGL emission proves to be too faint to be measured in this set of data. Using the predictions given in the FOC Handbook, we estimated the maximum DGL contribution to the FOC background counting rate. It is four times lower than the mean background dark noise measured in our data set. The mean dark noise is $9 \times 10^{-5}$ counts/pixel/second. The sky components have been measured as functions of the relevant spacecraft angles, i.e. the solar zenith angle, the target zenith angle, the target-to-Sun angle, and the ecliptic coordinates for the object and the Sun. The measurements have been compared with predictions derived from atmospheric models. The zodiacal light is well within the expected range of 70-210 S10 units for the observed ecliptic coordinates. The Lyα emission background is 25 percent lower than expected for all solar zenith angles. The OI data are at least 50 percent higher than the predicted OI counts. There is a weak correlation between the Lyα emission and the target zenith angle.

The complete paper reporting in detail these measurements and results with figures has been submitted to the Astronomical Journal (Caulet, Hook, and Fosbury, October 1993).

---

1. ST-ECF, ESO, Garching, Federal Republic of Germany.
2. affiliated to the Astrophysics Division of ESA.

# The Calibration Data Base for the Hubble Space Telescope

Colin Cox [1] and Calvin Tullos [1]

**Abstract**

We discuss the requirements and design of the calibration data base which supports the processing of Hubble Space Telescope observations. We describe procedures for ensuring that, despite the continuing changes to software and hardware, calibration data to match the instrument configuration for any observation are provided when needed.

## I. Introduction

The Hubble Space Telescope has six astronomical instruments that are continuously attached, and must be considered as part of the telescope. Following the installation of the Corrective Optics Space Telescope Axial Replacement (COSTAR) we will have one less because the High Speed Photometer will be removed. Calibrating the telescope really means providing calibration information for the optical assembly itself, two cameras, two spectrographs, and the Fine Guidance System. Each of these instruments may be operated in a number of modes involving such things as selection of optical paths to different detectors, use of various filters and data collection formats. For each of these instruments there are between seven and seventeen different types of calibration to be supplied and related to multiple instrument modes. As an example, flat fields are supplied for the Faint Object Spectrograph. The flat field to be used depends on which of two detectors, nine dispersers and eleven apertures were selected for an observation. If the apertures were paired then there is a choice between upper and lower positions and if a polarizer is chosen, there is a flat field particular to each polarization direction.

## II. Calibration of Observations

The calibration data are used in the Post Observation Data Processing System (PODPS), a software pipeline which automatically applies the basic data reduction to incoming observations. As an example, a calibration sequence for the Wide Field and Planetary camera is:

1) Apply a static defects mask to the image.
2) Flag saturated pixels.
3) Fix up a known problem with the Analog to Digital converter hardware.
4) Subtract a DC bias level for each detector.

---

1. Space Telescope Science Institute, Baltimore, MD 21218

5) Subtract a bias image.
6) Subtract a pre-flash image.
7) Subtract a superpurge residual image.
8) Subtract a scaled dark count image.
9) Apply a flat field correction by multiplying by an inverse flat field image.
10) Generate a histogram of the image intensities.
11) Scale the final image according to the format of output needed.

All steps except 3, 10 and 11 require access to calibration images, several of which are time dependant. There are separate sets for the Wide Field Camera and the Planetary Camera. The superpurge and flat fields depend on the filter combination in use. To enable all these steps to be performed, PODPS maintains a data base containing the currently applicable calibration data extracted from the main Calibration Data Base (CDB).When an observation data file arrives, the names of the required calibration files are determined from the instrument name and its observation configuration. A check is performed to ensure the files are present and, if so, the file names are placed in a header file. If no file has been cataloged for the particular configuration the name remains blank and an error message is issued. If the file is named but is missing, again an error message is logged. The calibration step attempts to proceed in any case, reading and applying the files indicated in the header. In the event of problems, the calibration steps that can not be completed are omitted and the raw and partially calibrated data are forwarded to a trouble area instead of being delivered to the observer. Problems are usually resolved within one day and the calibration re-run with appropriate data or, if necessary, with the problem step omitted.

The Calibration Data Base is designed principally to support the PODPS pipeline processing. Additionally, it provides data for off-line calibration both for checking or correcting pipeline calibrations and calibrating archival data. Thousands of calibration files have to be supplied, cataloged and occasionally updated. The pipeline must maintain copies of all files that might be needed and be able rapidly to locate those needed for the incoming observations.

To these ends, the data base retains all calibration data submitted, including some which was not delivered to PODPS. When the telescope was launched in 1990 the calibration data consisted of laboratory measurements and some purely nominal values such as flat fields containing all ones. As we have operated the telescope, made measurements and learned more about the performance of each instrument, calibration data files have been updated many times. We maintain a complete history of every file submitted and the checks performed at each stage. For any given observation we are able to supply a list of the currently most appropriate calibration files to use. In some cases this list may differ from the list PODPS used because improved calibrations have been obtained since the observation.

The data base is maintained on a Sun system running Sybase relational data base software. The data and pointers are held here while the bulk data are kept on a large scale optical disk system, the Data Management Facility (DMF). We have approximately 8 Gigabytes of data in hand at present, about 95 percent of it being for the Wide Field and Planetary Camera. The tools to populate and process the data base are part of the Space T elescope Science Data Analysis Software (STSDAS). Files are transferred from a local V AX to another associated with the optical disks via Decnet over ethernet. Figure 1 shows the various sub-systems and the flow of information.

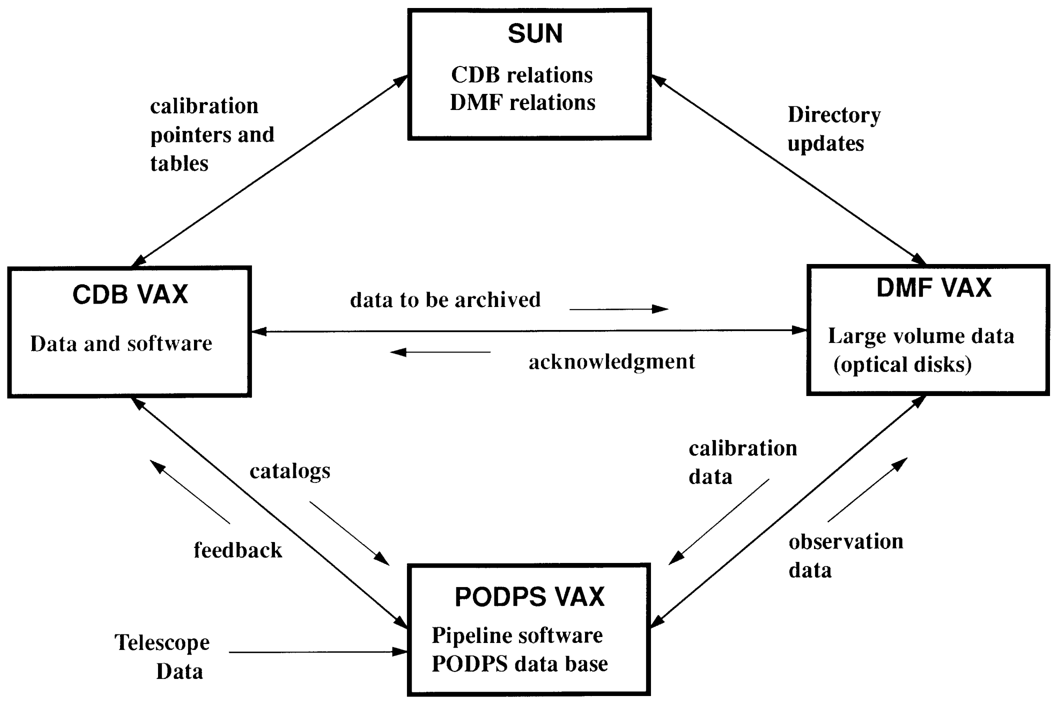


**FIGURE 1. CALIBRATION SYSTEMS AND DATA FLOW**

## IV. Data Delivery Procedures

When we in Calibration Operations receive a set of calibration data files we have to prepare them for submission to PODPS. Along with the files comes a table, in each row which are specifiers for a single mode of the instrument being calibrated, plus either the associated data or the name of a file containing the data. If the data consist of a small number of elements they will be directly in the table, but if the data is an image, then the image name will be present. Figure 2 illustrates the steps taken to supply a new calibration file to PODPS. The files are supplied by the Investigation Definition T eam (IDT), the Science Instrument Branch (SIB) at this institute. W e run some preliminary checking of the files to see that the format is correct and the required keywords are in place. The next thing we do is to give the files a new and unique name derived from the current date and time and incorporating codes for the instrument and type of calibration. The table also gets renamed, and the names inside the table reflect the new unique values. For a given type of calibration, there exists a table with a row for every file that has been submitted. This includes multiple entries for identical configurations which may have been updated several times. In the data base there exists a relation for every type of calibration which maps the calibration table, and as we incorporate each new set of data the corresponding relation is augmented.

PODPS requires just the latest version for each configuration. W e call the table which contains the latest version of each configuration, a catalog. A new catalog is generated in which the new data replace some of the rows. At this stage the new file names are announced to the deliverer who is required to test the files on software which emulates the pipeline.

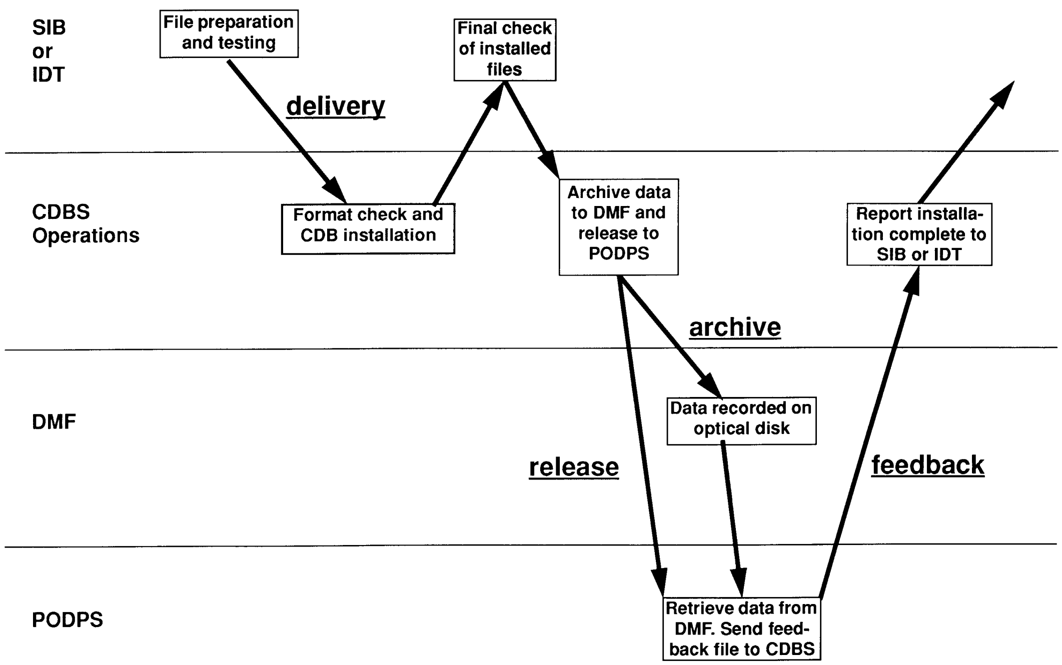


**FIGURE 2. CDBS DELIVERY FLOW**

Once these tests are passed and signed off, we update a verification relation which records this fact, along with the time and a version number . We next send the files to the DMF V AX, and operators there place them permanently on optical disk. W e then run a release program which examines the verification relation, checks that the data have been installed on DMF , and if all is well, forwards the catalog to PODPS. As part of this procedure, other relations are updated giving the time of delivery and the catalog name. PODPS personnel in turn retrieve the new files from the DMF optical disks to magnetic disk, replace their catalog and delete any files which have been superceded. So the catalog takes a direct path while the data a much more roundabout one. PODPS returns to us, what we call a feedback file, which confirms that they were able to retrieve from the DMF the files listed in the catalog. Finally we update yet another relation to track the time of installation and inform the deliverer that the files are in place. The means of supplying the data to PODPS may seem rather roundabout as opposed to forwarding files directly . The reason for doing it this way is principally to ensure we have a reliable archive. Nothing is ever deleted from optical disk nor from the relations of the Calibration Data Base. However , neither we nor PODPS retain all the calibration files on our own magnetic disks; they would soon overflow the available disk space.

## V. Time Dependent Calibrations and the USEAFTER Date

In general, the most recent calibration for a given instrumental mode is the preferred one because the usual reason for updating the calibration is that the data have been replaced by the results of improved measurements. There are many cases for which this is not the only consideration because the changed values represent a real change in the instrumental performance. The sensitivity of the Faint Object Spectrograph has changed by more than 10 percent over part of the spectral range. From time to

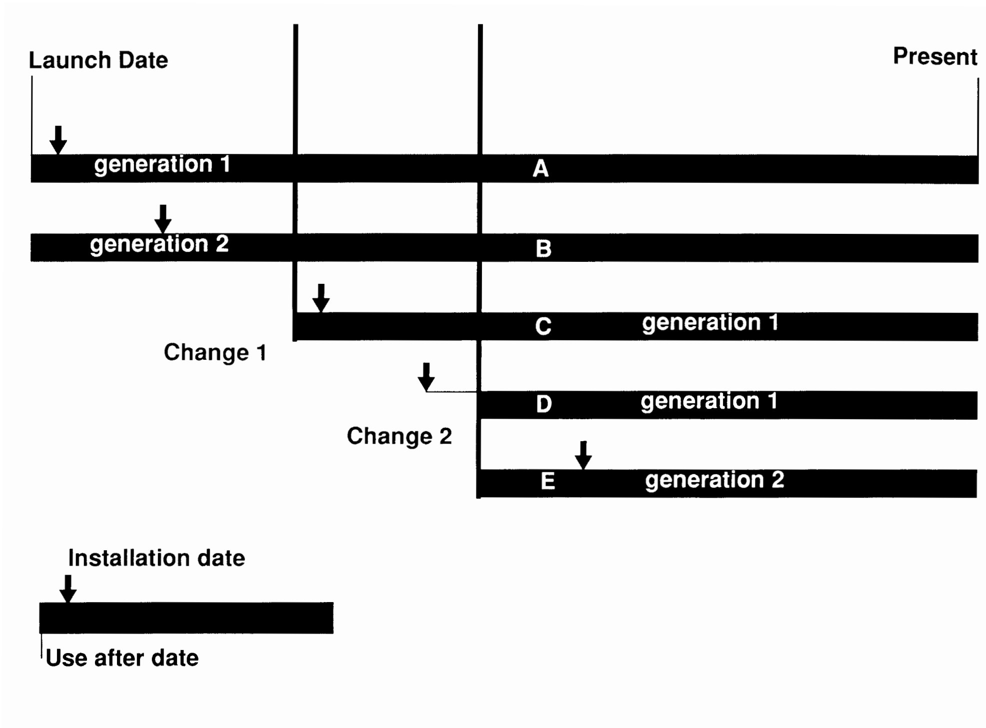


**FIGURE 3. THE USE-AFTER DATE**

time diodes cease to function and we update the Dead Diode tables. In these situations, and when analyzing observations which are not current, it is important to have access to previously entered files and to use the calibration closest in time to that of the observation. W e therefore associate a date with each calibration with the meaning, “use only on observations taken after this date”. For calibration data which simply reflect improved knowledge, the starting date should be the same as that of the data being superceded. There is no recorded ending date because at the time the data is entered the length of time for which the data will be valid is unknown. Replacement calibrations with the same starting date are distinguished by a generation number . Then the calibration to use is the one with the highest generation number and the latest “use after” date which is not later than the observation date. To determine the correct calibration to use, a search of the data base selects all entries which exactly match the instrument configuration of the observation and have "use after" dates earlier than that of the observation. From these, the entries with the latest date are chosen and finally , within this set, the one with the highest generation number is selected.

Figure 3 illustrates how the "use after" date operates in several cases. The top line represents an initial data set installed shortly after launch but applying to all observations from the date of launch. The results of some in-flight measurements permit improved calibrations to be installed at a later date. Line B with generation number 2 supersedes line A. Any recalibration of the earliest observations would use the new calibration. At a later date, a real instrumental change is detected and line C shows the new installation which should be applied only to observations taken after the change date. Line D illustrates the possibility of installing a calibration in anticipation of an instrument change, such as the activation of COST AR while line E corresponds to the updating of calibration D.

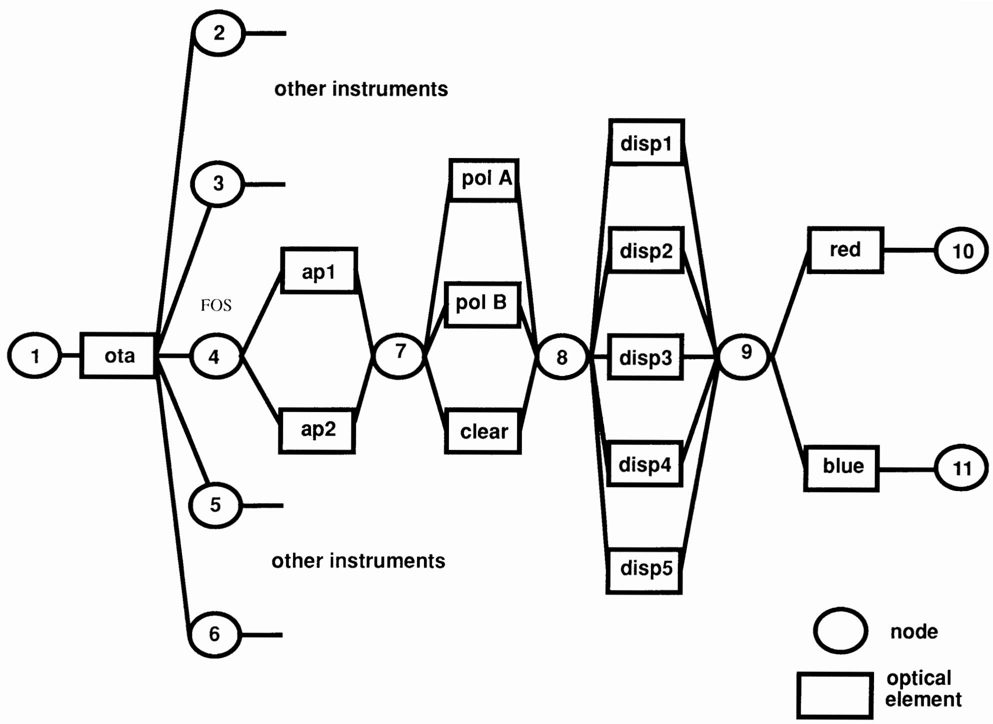


FIGURE 4. AN INSTRUMENT GRAPH

## VI. Throughput Model

The sensitivity of any observational mode of the telescope obviously depends on the optical path, specifically , what filters, detectors and apertures were used. There are theoretically tens of thousands of possible modes of which a hundred or so are actually in use. Many of the usable modes have much in common, in many cases only differing by one filter element. T o accommodate this complexity without having to maintain data for every conceivable combination, the throughput calculations are based on a graph representation of the optical path. Figure 4 illustrates a section of the telescope graph including a simplified graph for a hypothetical instrument similar to the Faint Object Spectrograph. The graph represents a choice of two apertures followed by the optional inclusion of a polarizer with two polarization directions, a choice of five dispersers and finally one of two detectors. A path is defined by a list of optical elements in the order that the light passes through them. Each element has its own throughput function which is a light transfer ratio as a function of wavelength. At the end of each path the detectors have a wavelength dependant quantum efficiency. The total throughput for any optical path is then the product of the throughputs of each element in the path. Even in this simple example, 60 possible paths are supported with only 12 throughput tables. There are, of course, complications related to interpolation when different elements are calibrated on differing wavelength grids, and it is not always possible to isolate the effect of every element.

To support this model, the CDB contains several different types of files and tables. The overall telescope graph which defines each component and its connections is described by numbering each node in the graph and attaching a meaningful name to every arc in the graph. A single optical path is a sequence of arcs for which the exit node of one element is the entrance node of the subsequent element. Each path is given a name. Then the graph table is a table containing columns for component name, path name, entrance node and exit node, the numbers of the nodes at each end of the arc. Most components will appear many times as they belong to many paths. To trace a particular path, the software begins at the first node and looks for an element which has that as the entrance node and is associated with the path name. Then the corresponding exit node is used as the new entrance node and the search continues until a detector is reached, collecting the list of components along the way.

A second type of table lists the component names along with the name of the table containing the actual throughput data, essentially an index pointing to a third type of table.This third table is a list of wavelengths and corresponding throughput ratios or, in the case of a detector, the quantum efficiencies. To calculate a path's overall throughput or sensitivity, the list of components along the path is used to select the individual tables. The product of transmission factors provides an overall wavelength sensitivity. Multiplying this by the spectrum of an observed object provides an output spectrum and an integrated count rate. This software is used in the pipeline for the Faint Object Camera and the High Speed Photometer. It is also being incorporated into the software for the second generation Wide Field and Planetary Camera (WFPC2). More commonly the software is used off-line in planning observations and preparing proposals.

It is clearly quite convenient to accommodate changes to throughputs or sensitivities by updating throughput tables. Another advantage that will become apparent as we prepare for the refurbishment mission in December is that adding new elements requires no software change. The corrective optics assembly that will be put in place adds two small mirrors to the optical paths of the Faint Object Camera, the Faint Object Spectrograph and the High Resolution Spectrograph. We will add these elements to the graphs, define new optical paths which include the new mirrors, and provide throughput tables for the new components. For the spectrographs certainly there will be other changes because the better focussed beam will pass a higher proportion of its light through the smaller apertures than before. Again this will be included by changing the matching tables.

In addition to the tables described which directly support the throughput software, the CDB retains a catalog of basic reference data that were compiled for building the tables. This includes photometry and spectra of standard stars plus polarization standards and line profiles. All of this data is referenced by data base relations so that qualified searches may be made. This, like the rest of the calibration data, is available to the general observer .

## VI. Summary

The overall system now works extremely well. It is rare that PODPS is unable to locate a reference file that it needs. Occasionally it happens that an unusual instrumental mode is used for which there is no table entry . Perhaps a previously unused filter combination arises for which no flat field exists. Normally we can use an existing file, but if not, the data can be passed through, omitting a step in the calibration. If a file becomes available later , the observation can be re-processed off-line using the STSDAS software. Equivalents of the pipeline calibration are available for all instruments. Both the calibrated and uncalibrated observation data are always supplied to the principal investigator . All calibration data is available on request to any observer .

We encountered a number of complications during 1992 because we were involved in a re-processing effort. The software had seen some significant improvements in the time since launch, and we decided to re-process most of the previous two years' observations. So throughout 1992 we were running a system parallel to PODPS which was working on old observations while PODPS itself operated on current observations. The two systems had to share access to data and be able to sort out which calibration files each should use. It was during this period that we instituted the "use-after date" scheme. This allowed the re-processing pipeline to point to old calibration files while the PODPS pipeline picked up the current ones.

This same mechanism will be of considerable value when we activate the COST AR. To effect a smooth change-over we will need to be prepared with post-COST AR calibration files even while we are still calibrating pre-COST AR observations. The new data will be in place in the DMF but only released when we know exactly when the COST AR mirrors are to be activated. This will be on different days for each instrument and will await the completion of many tasks. The applicable USEAFTER date will correspond to the day of the mirror activation and need only be chosen at release time.

# Post-Observation GO Support

Krista Rudloff [1]

## I. Research Support Branch

The Research Support Branch (RSB) at STScI is responsible for post-observation General Observer (GO) support. While most GOs are familiar with the pre-observation support provided by the User Support Branch (USB), GOs should also be aware of the resources that RSB has to offer. These include data analysis support for both visiting and remote GOs who have *HST* data.

## II. How Can We Help?

We encourage all *HST* GOs (especially first time GOs) to visit the Institute at least once to learn how to analyze their data. A Science Data Analyst (SDA) is assigned to each visiting GO and is available to help the GO throughout the entire visit. Our staff of SDAs is very knowledgeable about all aspects of *HST* data and can answer questions that GOs typically have. During the visit, the SDA serves as the prime contact for the GO, acts as a tutor for the GO, and can also arrange meetings with the instrument scientists or refer the GO to other staff experts in a variety of subjects. SDAs can provide tutorials in UNIX, IRAF, and STSDAS if necessary. They can also teach GOs about Routine Science Data Processing (RSDP), re-calibration, deconvolution, and post-reduction analysis for each of the instruments.

## III. Visiting the Research Support Branch

A typical visit lasts about a week, but if the GO is unfamiliar with IRAF or STSDAS, we recommend a longer visit. Prior to a visit, the SDA Coordinator (Krista Rudloff, rudloff@stsci.edu, 410-338-5013) assigns an SDA to the GO and sets up a temporary computer account for the GO to use. The SDA Coordinator also contacts the GO to assess their needs and goals, and with proper authorization, will load the data (within reasonable volume limits) that the GO wishes to work with during the visit. The assigned SDA prepares for the visit by checking that the account and all hardware and software are functioning properly, as well as checking the quality of the GO's data. This allows the SDA to foresee possible problems or additional needs. Due to this thorough preparation, we request two weeks advance notice for a visit. Data analysis support can also be obtained remotely. Remote GOs are encouraged to call or email RSB with questions they have about any of the topics discussed above.

If you have questions about the analysis of your *HST* data, or would like to arrange a visit, you can contact RSB via email (analysis@stsci.edu) or phone (410-338-1082).

---

1. Space Telescope Science Institute, Baltimore, MD 21218

**White Dwarfs as Absolute Flux Standards**

David S. Finley [1]

**Abstract**

Hot DA white dwarfs can serve as excellent calibration sources through the far ultraviolet (FUV) and visible spectral regions. Accuracies of temperature and gravity determinations and of modeling are such that the relative flux may be predicted for an individual star with an accuracy of typically better than 2 percent. By making certain restrictions, the relative fluxes can easily be determined to better than 1 percent. The absolute flux level is determinable by visible photometry or spectrophotometry to an accuracy of 3 percent or better . Thus the overall accuracy of the calibration that can be provided by white dwarfs is dominated not by errors in parameter determinations or flux modeling, but rather by observational uncertainty in the absolute fluxes in the visible.

## I. Motivation

Hot DA white dwarfs are the most suitable class of object for use in absolute flux calibrations. Their atmospheres consist of pure (or nearly pure) hydrogen. Number abundances for He are typically $< 10^{-5}$ with respect to H, and even "metal rich" DA have total heavy element number abundances that are $< 10^{-4}$ relative to H. The atmospheres are plane-parallel, and there are no detectable winds. The atmospheres do not significantly depart from LTE; the only NLTE effects seen are very narrow features in the H line cores that are only observable at high resolution. Above about 16,000 K, convection becomes negligible. Above 20,000 K, the quasi-molecular Lyman α satellite features that are peculiar to DA below 20,000 K disappear. Furthermore, the bright WD that are suitable for calibration purposes ($V \sim 13$) are also nearby , and have negligible reddening ($N_{HI} < 1\times10^{19}$ cm$^{-2}$). The purity of the DA atmospheres is such that the only spectral features detectable are the H lines; outside those lines, a very pure continuum is obtained (excepting the metal-rich DA above about 50,000 K).

Historically , an early suggestion that white dwarfs could serve as useful primary flux standards for *IUE* was made by Greenstein and Oke (1979). Later , a correction to the *IUE* flux standard based on white dwarfs was presented by Finley , Basri and Bowyer (1990). White dwarfs have now been used by the *IUE* Project to establish the relative flux scale for the *IUE* calibration (González-Riestra et al, this volume). White dwarfs were also used for the calibration of the Hopkins Ultraviolet Telescope (Kruk, this volume). An outcome of this meeting has been a decision to obtain spectra of

1. Center for EUV Astrophysics, 2150 Kittredge Street, University of California, Berkeley , CA 94720

additional white dwarfs for the purpose of improving the absolute calibration of the *HST* FOS.

The purpose of this presentation is to demonstrate that these calibration efforts rest on a sound theoretical footing, and that the use of the white dwarfs for calibrating critical instruments will not introduce any systematic biases in the flux scales.

## II. Accuracy of Flux Predictions

The technique suggested for obtaining absolute fluxes for white dwarfs consists of determining accurate temperatures and gravities by detailed fitting of the hydrogen line profiles (Balmer , and L yman if available), generating synthetic spectra using model atmospheres for those input parameters, and scaling the model spectra to match visible photometry or spectrophotometry . Thus there are two error terms: a slope error , due to the uncertainty in the temperature determination, and a "zero point" error , due to the uncertainty in the visible photometry or spectrophotometry used to set the absolute level. (Gravity errors affect the relative fluxes by less than 0.3 percent above 30,000 K).

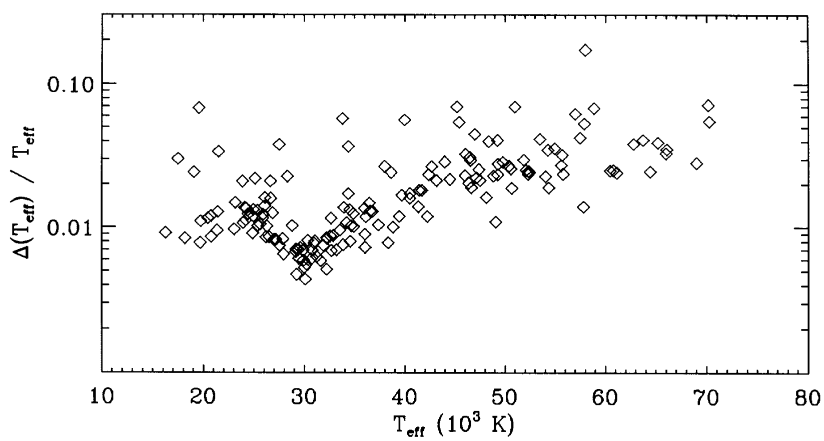


Figure 1: Fractional $T_{eff}$ error obtained from Balmer line profile fitting for our sample of hot DA white dwarfs.

A real-world example of the temperature determination accuracy that is obtainable is shown in Figure 1, which is a plot of the fractional 1 $\sigma$ errors obtained from fitting the Balmer line profiles for 170 hot DA white dwarfs that I observed with typically 100:1 S/N at 5 Å resolution. Errors are derived from $\chi^2$ analyses, and are due to the S/N of the spectra. In most cases, parameters are obtained from simultaneously fitting H $\beta$, $\gamma$, $\delta$, and $\epsilon$. The $T_{eff}$ errors range from significantly less than 1 percent at 30,000 K to about 3 percent at 60,000 K. Some fraction of the targets were less well observed, and have significantly larger errors for their temperatures than the typical values. Note that the brighter objects that are best-suited for calibration purposes have temperatures that are determined much more accurately than in the "typical" cases.

The largest error in the predicted flux is in the FUV , so I have calculated the error in the predicted flux at 1400 Å relative to the flux at 5490 Å (the isophotal wavelength for the Johnson V band) for the same set of objects, given those temperature errors.

The result is plotted in Figure 2. It is seen that as long as the temperature range is restricted to ≥ 27,000 K, the error in the predicted 1400 Å flux (relative to the visible) will typically be of the order of 0.5 percent to 1.5 percent.

The wavelength dependence of the predicted flux error is shown in Figure 3, in which I have plotted the ratio of the model flux for $T_{eff}$ = 51,000 K so that for a 50,000 K model, representing a fairly typical 2 percent $T_{eff}$ error for that temperature range. The errors are negligible in the Paschen continuum, are less than 0.5 percent at the red end of the Balmer continuum, and monotonically increase toward shorter wavelengths to about 1 percent in the vicinity of Lyman α.

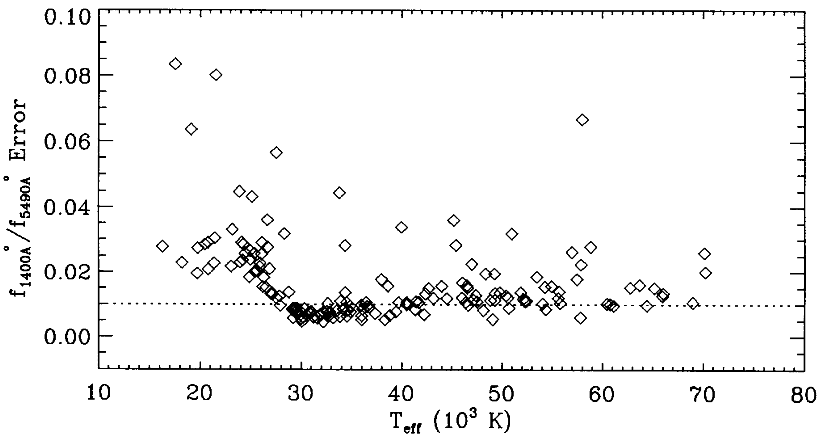


Figure 2: Error in predicted flux at 1400Å relative to flux at 5490Å based on $T_{eff}$ errors shown in Figure 1.

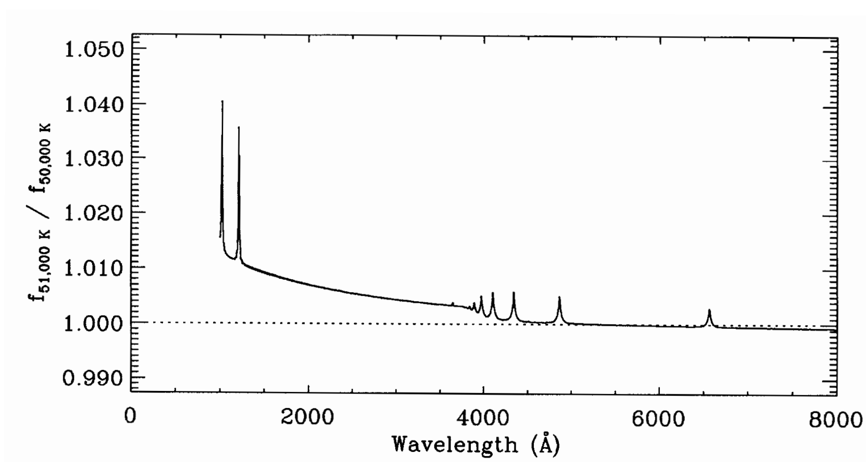


Figure 3: Relative flux error vs. wavelength (normalized at 5490Å) given a 2 percent error in $T_{eff}$ at 50,000K

## III. Systematic Errors

The above results show that the internal errors in the effective temperatures obtained from Balmer line profile fitting are such that the relative model fluxes we predict will be in error by at most about 1.5 percent at the shortest FUV wavelengths, and much less than 1 percent in the optical. Those accuracies are obtainable for DA white dwarfs with effective temperatures ≥ 27,000 K. However, there are also external, systematic effects that can affect the results.

Due to the advent of modern detectors on medium to large telescopes, we now commonly obtain spectra for white dwarfs fainter than 16th magnitude with S/N exceeding 100:1. This has led to the realization that the current treatment of Stark broadening in the higher Balmer lines is not completely satisfactory (Bergeron 1993, Bergeron, Saffer and Liebert 1992). The wings in the higher lines are predicted by current theory to be too strong, thus requiring lower temperatures to achieve a fit, relative to the lower Balmer lines. (This is only a few percent effect in the Balmer lines, which is why it was not noticed in the days of lower S/N optical spectra). A provisional method for removing this inconsistency, in lieu of the development of a more sophisticated Stark theory, has been suggested by Bergeron (1993). The method consists of, in effect, doubling the strength of the field due to adjacent charged particles that is required to "dissolve" a given atomic level of hydrogen. The relevant parameter employed in the Hummer-Mihalas occupation probability formalism (Hummer and Mihalas 1988) is referred to as $\beta_{crit}$. Doubling that parameter has the effect of reducing the probability of finding electrons in quasi-bound states, thus reducing the strength of the pseudo-continuum that overlies the Balmer line series. Functionally, that has the same effect as reducing the strengths of the overlapping wings of the Balmer lines, and allows consistent fits to be obtained for the full Balmer series. (It remains to be conclusively shown whether or not that approach introduces any significant systematic biases in the temperatures and gravities obtained).

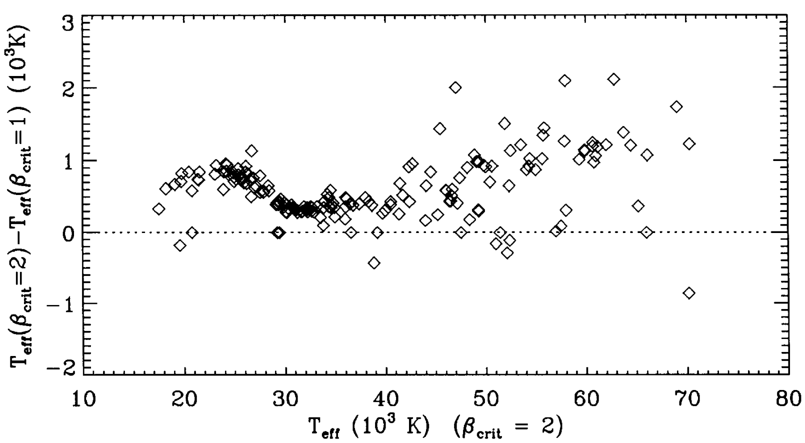


Figure 4: $T_{eff}$ differences obtained from fitting Balmer line profiles using models with $\beta_{crit}$ = 1 or 2.

The question of the proper Stark broadening treatment (or Hummer-Mihalas parameter values) to use is being addressed by the author's ASTRO-2 program that will involve the observations of the full Lyman series for several hot DA white dwarfs. The effects in the Lyman lines are expected to be several times larger than in the Balmer lines, thus allowing fine tuning of the Hummer-Mihalas formalism and testing of new, improved Stark broadening theories. However, for now, we can obtain an overestimate of the effect of the Stark uncertainties on the predicted fluxes by comparing the results obtained for $\beta_{crit}$ = 1 with those obtained for $\beta_{crit}$ = 2. (The values ultimately obtained after the Stark question is settled are expected to be much closer to those we obtain with $\beta_{crit}$ = 2). A check was made by deriving $T_{eff}$ and log $g$ for the full sample of objects described above, using both values of $\beta_{crit}$ and (usually) simultaneously fitting H$\beta$, $\gamma$, $\delta$, and $\epsilon$. The differences in $T_{eff}$ are shown in Figure 4. Temperatures obtained with $\beta_{crit}$ = 2 are consistently higher than for $\beta_{crit}$ = 1, by several hundred K just above 20,000 K, decreasing to a few hundred K around 30,000 K, and slowly increasing to about 1000 K around 60,000 K.

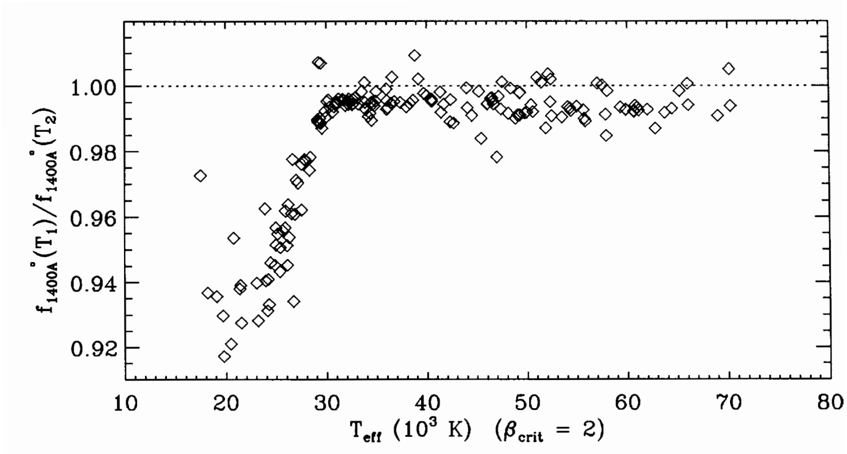


Figure 5: Ratio of FUV fluxes (normalized to 5490Å) for $\beta_{crit}$ = 1and 2. T $_1$ refers to T $_{eff}$ obtained for $\beta_{crit}$ = 1etc.

The effect of that temperature difference on the predicted FUV flux (relative to the visible) is shown in Figure 5. For the temperatures obtained for a given value of $\beta_{crit}$ we used the models for the same value of $\beta_{crit}$ to predict the fluxes at 1400 Å (normalized in all cases to 5490 Å). For each object, we then calculated the ratios of the normalized 1400 Å fluxes based on the different values of $\beta_{crit}$. It is clear from Figure 5 that above about 30,000 K, the systematic error in the predicted fluxes that is due to the current uncertainty in the Stark broadening treatment is no more than 1 percent. However, given the rapid increase in the systematic (and random) errors in the predicted fluxes below that temperature, we suggest a lower limit of about 30,000 K for white dwarfs that are to be used for high precision absolute flux calibrations.

## IV. Metals

The question of the presence of metals in white dwarfs invariably arises in the context of considering white dwarfs as flux standards. Previously, our knowledge of that subject was rather limited. Now, however, we have the two EUV all-sky surveys, by the *ROSAT* Wide Field Camera (WFC) and by the Extreme Ultraviolet Explorer (*EUVE*), and most importantly, we now have *EUVE* spectra of a significant number of hot DA white dwarfs. We now know that those DA WD that are heavily absorbed in the EUV have significant concentrations of trace elements; metals are essentially ubiquitous in the region of the $T_{eff} - \log g$ plane above about 50,000 K and below $\log g \sim 8$. Furthermore, the distribution of relative abundances is apparently consistent with the presence of metals being due to radiative support.

Metals have a profound effect in the EUV, where overlapping bound-free continua and line blanketing start reducing the flux below about 260 Å. G191-B2B is one of the DAs that has the highest concentrations of heavy elements, and its flux at 100 Å is reduced by 4 orders of magnitude relative to a pure H DA of the same effective temperature. The effects outside the EUV are much more subtle, though. Models with metals do not accurately reproduce the hydrogen line profiles unless, in addition to the bound-free opacity that dominates the EUV spectrum, one also self-consistently includes hundreds or thousands of metal lines that lie in the EUV and FUV and provide significant cooling that counteracts the upper atmosphere heating caused by the bound-free opacity . Models that have that capability are in progress. Furthermore, metals (particularly of the Fe group) have large numbers of lines that can overlap and reduce the apparent continuum level. This is shown in Figure 6, which includes the flux for a 60,000 K, log $g$ = 7.5 model that matches both the Balmer line profiles and the observed continuum flux level for G191-B2B, and a 57,000 K model that includes a few hundred of the strongest Fe lines, with an abundance of Fe/H = 3 $\times 10^{-6}$, as well as C. (Note that the CIV doublet at 1550 Å is unresolved, given the assumed instrument resolution of 3 Å FWHM. Also, note that the metal spectrum has been lowered by 0.5 percent so that the continua of the two spectra overlap.) Thus, in the more metal rich DA, we can expect to have some portions of the EUV spectra reduced by order of a few percent due to overlapping metal lines.

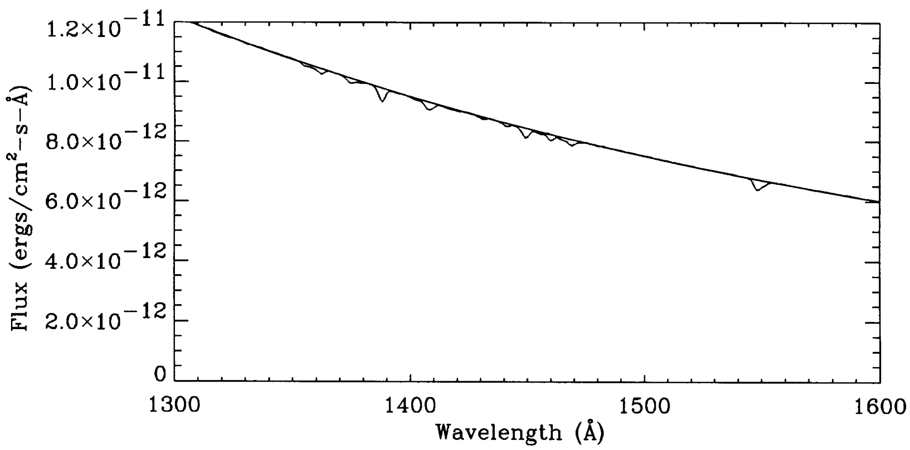


Figure 6: Pure H model, 60,000K, and metal-rich model, 57,000K, including a few hundred of the strongest Fe lines, and the CIV 1550Å doublet. Metal model spectrum is shifted downward by 0.5 percent, and convolved with instrumental resolution of 3Å FWHM.

## V. Recommendations

At effective temperatures below 30,000 K, the Balmer continuum slope starts becoming a more sensitive function of $T_{eff}$, without a corresponding increase in the accuracy of the temperatures obtained from Balmer line profiles. Thus, the internal uncertainty in the predicted FUV flux at 1400 Å rapidly increases from about 0.5 percent at 30,000 K to at least a few percent at cooler temperatures. Furthermore, the systematic errors due to uncertainties in the current treatment of Stark broadening and the hydrogen equation of state are such that systematic errors in the predicted FUV fluxes may approach several percent below 30,000 K.

Above 50,000 K, metals are apparently nearly always present. Although the case of G191-B2B suggests that even for very metal-rich DA, one may use pure H Balmer fit temperatures to model the relative fluxes to an accuracy of a few percent or better , prudence suggests that DAs hotter than 50,000 K should only be used as secondary standards, or avoided altogether, until fully self-consistent models including large numbers of metal lines are in hand, and fairly accurate abundance determinations have been made.

If one restricts potential DA WD calibration standards to the range of about 30,000 K to 50,000 K, though, the results shown here indicate that by determining $T_{eff}$ from high S/N optical spectroscopy, relative fluxes may be predicted with accuracies of 1.5 percent or better. Furthermore, the uncertainties in modeling hydrogen (of which we are currently aware) are such that systematic errors in the predicted relative fluxes should be less than 1 percent in this $T_{eff}$ range. Given an assumed accuracy of 3 percent for the absolute flux level as set by optical photometry or spectrophotometry, by selecting a sample of hot DA in the 30,000 K to 50,000 K range that have accurate visible fluxes and accurate temperatures, one can in principle establish an absolute flux standard from the red wing of Lyman $\alpha$ through the near IR with an overall accuracy of the order of 2 percent.

Much of the work described here is being carried out in collaboration with Detlev Koester. Additionally, all models discussed here were calculated using Koester's WD model atmosphere codes. This work was supported by NASA grants NAGW-2478 and NAS5-29298.

## References

Bergeron, P. 1993, in White Dwarfs: Advances in Observation and Theory, NATO ASI Series, ed. M.A. Barstow (Kluwer: Dordrecht), p. 267
Bergeron, P., Saffer, R. A., & Liebert, J. 1992, ApJ 394, 228
Finley, D.S., Basri, G., & Bowyer, S. 1990, ApJ 359, 483
Greenstein, J.L. & Oke, J.B. 1979, ApJ 229, L141
Hummer, D.G., Mihalas, D. 1988, ApJ 331, 794

# NLTE Extended Atmospheres of Massive Stars

D.J. Lennon [1], R.-P. Kudritzki [1,2], A.W.A. Pauldrach [1], R. Gabler [1] and S. Haser [1,2]

**Summary**

The UV calibration of the FOS, and by implication that of the primary flux standard ηUMa, are investigated by comparing FOS data for O-stars with the predictions of NLTE extended model atmospheres (both wind and unified models). A comparison with stellar wind calculations in particular , in which an attempt is made to synthesize the many lines due to iron group elements, supports previous suggestions that the present flux calibration can be improved. Furthermore, this improvement can be achieved through the use of detailed state-of-the-art model atmosphere calculations.

## I. Overview

The past few weeks has seen the completion of our *HST* program on *The Physics of Massive O-stars in Different Parent Galaxies* (P.I.: R.-P. Kudritzki) in which we obtained FOS G140H and G190H data for a total of 18 stars in the Large and Small Magellanic Clouds. One of the important aims of this program is to derive metal abundances, in particular for iron group elements, and to investigate the dependence of mass-loss rates upon these through application of radiation driven wind theory . Since the absorption lines of iron group elements are a dominant source of opacity in the UV it is important to establish the nature of this relationship, in particular if one wishes to extend this kind of work to more distant galaxies where an independent estimate of abundances is not available.

However, due to the serious line crowding problems in the UV for hot stars, we have to resort to spectrum synthesis in order to derive precise abundances. It is clear that for this kind of work we need reliable flux calibrations of the observational data, since one may not have a local continuum in the UV as a reference point. However , when we look at a comparison between observed and theoretical UV fluxes, for example Bohlin et al (1990: Figure 8), we see disturbing features at the 10-15 percent level as well as a general slope in the comparisons.

We show a similar picture in Figure 1 where we plot the flux ratio for ηUMa and an ATLAS6 model atmosphere, normalized to the V band. ηUMa is a primary flux standard upon which the current flux calibrations for FOS and *IUE* are based, thus one needs to establish the reliability of this calibration. It is important to realize therefore, that one of the most important developments in recent years for stellar

1. Institute für Astronomie und Astrophysik der Universität München, 81679 München, Germany
2. Max Planck Institut für Astrophysik, 85748 Garching, Germany

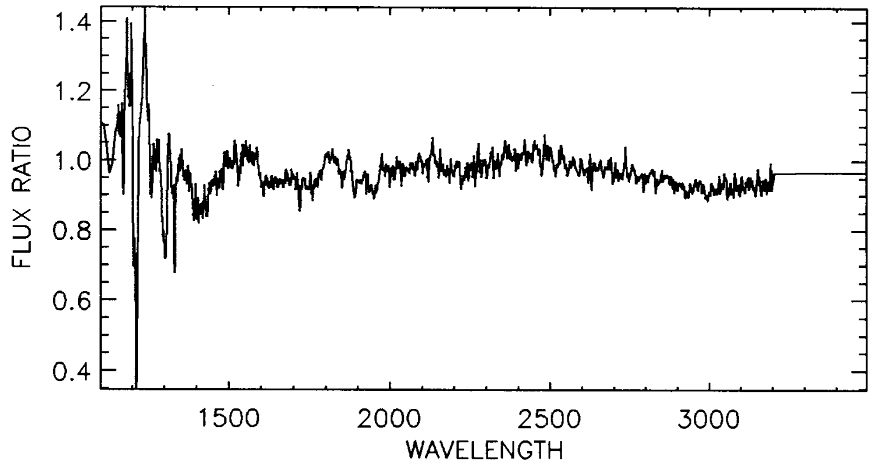


Figure 1: Comparison of η UMa and ATLAS6 model fluxes for an effective temperature of 17000K and log g = 4.25. Data are normalized to the V band and observed data are de-reddened assuming E(B-V) = 0.01.

atmospheres has been the great improvement made in both the quantity and quality of atomic data, especially for iron group elements. Thus it is now possible to compute synthetic spectra for hot stars with realistic line lists and opacities with which one can investigate these anomalies.

## II. Observational vs. Theoretical Spectra

Given the restricted wavelength coverage of our data, 1150-2300Å, we cannot address the problem of the perceived slope in the flux calibration. Futhermore, a comparison of our FOS data with *IUE* low dispersion data, shows that the former implies fluxes which are lower by up to 30 percent. Of course this may be due to a number of things; crowding in the *IUE* aperture, the *HST* PSF, centering problems in the slit. In addition, while all our stars have low extinctions (E(B-V) approximately 0.1), this is still significant when one considers that uncertainties of the order of 0.01 correspond to flux errors of 5-10 percent in the UV. (One must also consider different extinction laws.) For example, we show in Figure 2 a comparison of the observed, but de-reddened, data for the LMC O3 star SK-67211 with a unified model prediction, the atmospheric parameters of which were derived from fitting hydrogen and helium line profiles in the visible. The theoretical flux distribution was normalized to the observed V band. It is clear, given the uncertainties discussed above that little can be said about the general slope of the UV flux calibration from this data. We concentrate instead on the smaller scale features mentioned above, for example, the dips at 1400Å and 1600Å (see Figure 1).

We compare the predicted flux from a stellar wind calculation (including iron and nickel lines) with the de-reddened data for another LMC O-star Sk-67167 (O4If), see Figure 3. Note that we have normalized to the 1750Å region for this comparison. We can see that this appears to be a reasonable representation of the observed data (work is still in progress), however if we look closely at the 1400-1500Å region we see

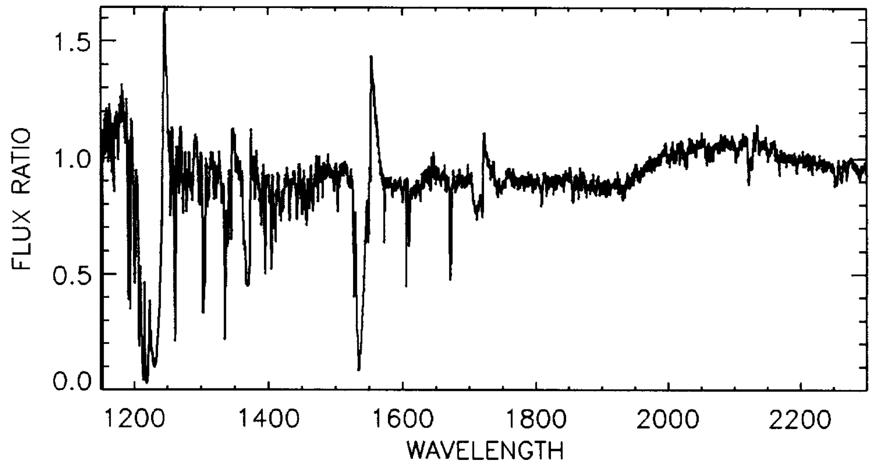


Figure 2: Flux ratio of de-reddened FOS data for SK-6721 1 and a hydrogen/helium unified model atmosphere flux distribution normalized to V . (Note that metal lines are not taken into account.)

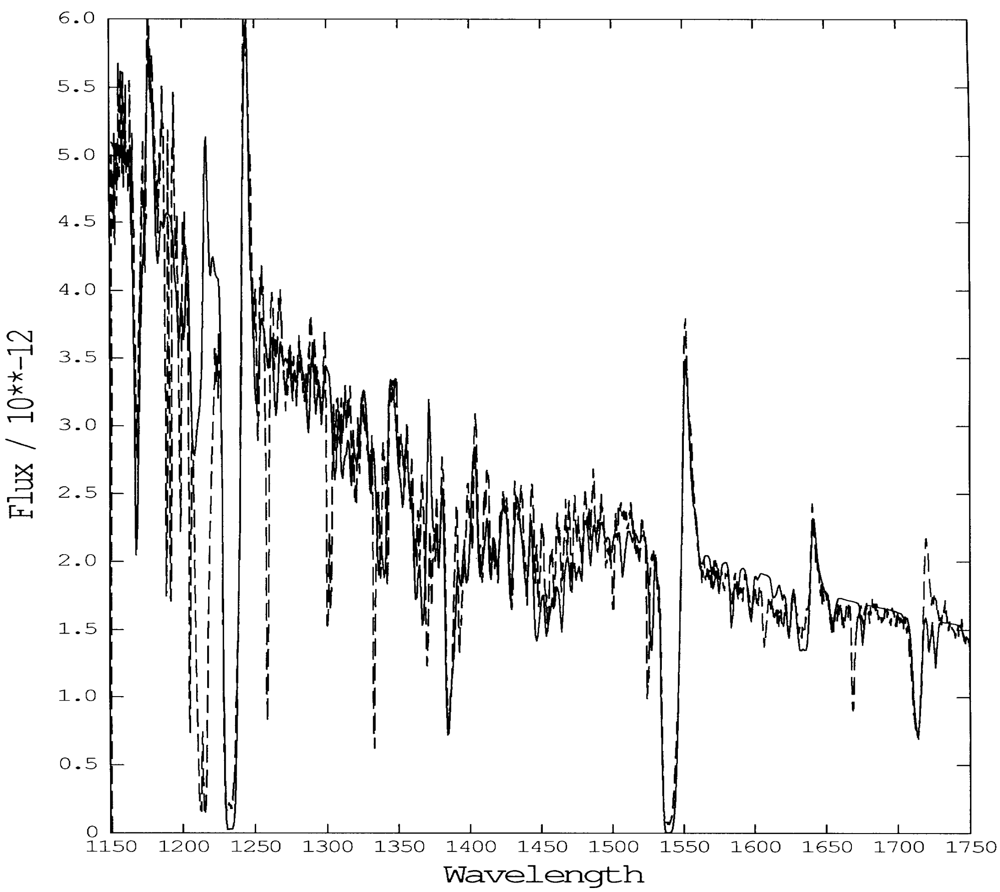


Figure 3: Comparison of computed (solid line) and observed (dashed line) flux distributions for Sk-671 67. Notice the apparent flux excess around 1450-1500Å

some discrepancies. These are more clearly illustrated in Figure 4 where we show the flux ratio binned into 10Å blocks and the flux excess (observed relative to model) around 1450Å is easily seen. Remembering that we normalized to 1750Å, one sees from Bohlin et al's Fig. 8 that one expects to find just such a peak. Clearly, if we wish to fit the iron lines in this region an improved UV flux calibration is extremely important. Conversely, one can also see from Figure 3 that in order to make reliable predictions of the expected UV flux for hot stars, it is necessary to account for the blocking caused by the many lines due to iron group elements with, for O-stars and supergiants, NLTE and stellar wind effects taken into account.

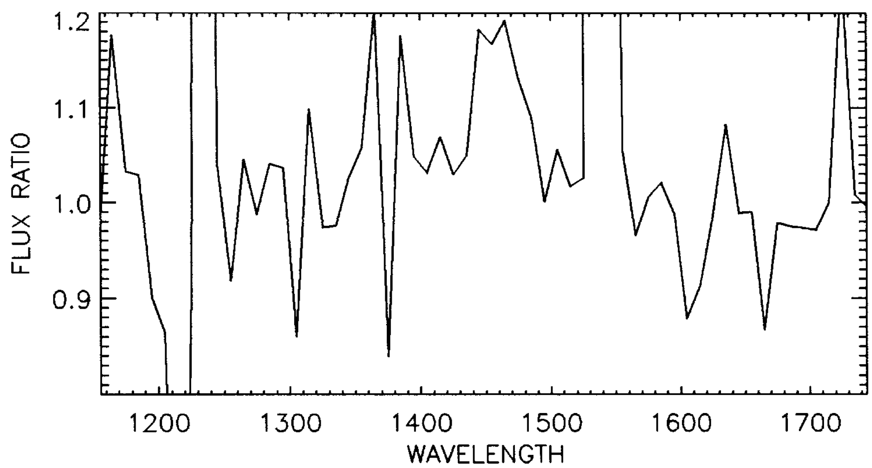


Figure 4: Flux ratio from Figure 3, binned into 10 blocks. Note the flux excess around 1450Å.

## III. Conclusions

From a comparison of synthetic spectra for O-stars based upon NLTE stellar wind calculations it appears that irregularities exist in the UV flux calibration used for FOS (and *IUE*) at the 10-15 percent level. We suggest that the use of realistic model atmospheres can help to identify and smooth out such features, and in this respect one should note the great improvements being made in this area for O-stars (Pauldrach et al, 1993) and for hot subdwarfs (Dreizler & Werner, 1993). Customized models for a few well-observed objects (such as the hot subdwarf G191B2B) would be of great value in achieving this objective.

It is a pleasure to thank Michael Rosa for bringing this problem to our attention and communicating his results prior to publication.

## References

Bohlin, R.C., Harris, A.W., Holm, A.V., Gry, C., 1990, ApJS, 73, 413
Dreizler, S. & Werner, K., 1993, AA, 278, 199
Pauldrach, A.W.A., Feldmeier, A., Puls, J., Kudritzki, R.-P., 1993, AA, in press

# The Photometric Calibration of the *IUE* Final Archive

R. Gonzalez-Riestra [1], A. Cassatella [2], H. Bushouse [3], D. Finley [4], A. de la Fuente [5], M. Garhart [3] and M. Perez [3]

## I. Introduction

The *IUE* data, with more than 95000 high and low resolution spectra available, is not only a powerful tool for scientific research, but represents also an important reference for the flux calibration of other space experiments. The *IUE* Final Archive project (see Nichols-Bohlin et al. 1993), now in operational phase for low resolution spectra, aims to a complete reprocessing of all *IUE* data using an upgraded image processing system (NEWSIPS), new Intensity Transfer Functions for the three cameras, and new accurate values for the parameters affecting the effective exposure times and the sensitivity of the detectors (e.g. camera rise/fall times, aperture dimensions, time sensitivity degradation, temperature dependence of the camera sensitivity, and the like). In this way, both the homogeneity and the internal accuracy of the *IUE* archives should be substantially improved. Equally important for the photometric accuracy of the *IUE* Final Archive is the redefinition of the absolute flux scale, as discussed in the following.

## II. The *IUE* Flux Scale

The initial *IUE* flux scale (Bohlin et al. 1980) is based on observations by other space experiments (basically *OAO-2* and *TD1*), each one affected by intrinsic systematic errors not well known at that time. In presence of discrepant measurements, and to force the convergence to a uniform flux scale (the $\eta$ UMa flux scale as established by Bohlin et al. 1980), the original measurements were suitably weighted and flux correction factors were provided for the *OAO-2* and *TD1* experiments (Bohlin and Holm 1984). The $\eta$ UMa flux scale is still being used by the *IUE* project as reference for the routine processing of *IUE* data (IUESIPS).

The *IUE* flux scale was not rediscussed until 1984–1985, when the project undertook the major task of obtaining a new set of ITF data for the three operational cameras SWP, LWP and LWR. These new data, together with an important set of observations of the usual *TD1* and *OAO-2* standards obtained in the same period, led to the recalibration of the three cameras, implemented in routine processing only for the LWP (Cassatella et al. 1992).

---

1. IUE Observatory, IUE-VILSPA, Madrid 28080, Spain
2. Istituto di Astrofisica Spaziale, CNR, I-00044 Frascati, Italy
3. CSC, IUE Observatory, GSFC, Code 685, Greenbelt, MD 20771
4. Center for EUV Astrophysics, Berkeley, CA 94720
5. VCS, IUE-VILSPA, Madrid 28080, Spain

The 1984-1985 recalibration phase, still based on the $\eta$ UMa flux scale, was essential to take an independent look at the problem of the *IUE* flux calibration, and provided the basis for a critical revision of the assumptions made in the original calibration. One of the by-products of the new calibration was the discovery that the fluxes of some of the classical *IUE* standard stars were inconsistent with the internal *IUE* flux scale. Others were excluded because of suspected variability or because they contained unevenly exposed spectra. All these stars were then excluded in the definition of the set of standards to be used for the flux calibration of the *IUE* Final Archive.

The impetus to revise the *IUE* flux scale was given by increasing evidence for repeatable discrepancies between observations and models of objects of very different physical nature such as white dwarfs (Greenstein and Oke 1979), and BL Lac objects and sdO stars (Hackney et al. 1982). More recently, Finley et al. (1990) showed significant deviations (up to 15 percent) when comparing *IUE* fluxes and fluxes predicted by models of DA White Dwarfs. The fact that the above deviations were maximum in the regions where the disagreement between the original *OAO-2* measurements and the *TD1* fluxes was maximum was a clear indication for the presence of systematic errors in the $\eta$ UMa flux scale.

Therefore, a major revision of the *IUE* flux calibration was considered a primary requirement at the moment of planning the activities inherent to the *IUE* Final Archive (Cassatella 1990). The fundamental basis of the recalibration plan was the intensive observational campaign carried out from VILSPA and GSFC in the period August 1990 to June 1991, intentionally limited in time to minimize the sensitivity variation of the detectors. The purpose was to obtain a statistically significant number of observations not only of the classical standard stars which the previous experience had shown to be the best, but also of a suitable set of hot objects including DA White Dwarfs and sdO stars. The list of WDs and sdOs was established in a meeting held at VILSPA in December 1990 attended by a small group of experts both on *IUE* calibration and in atmosphere modeling. As a necessary complement to this data set, several observations were made to test linearity, signal-to-noise ratio and repeatability, as well as to determine with the best possible accuracy all parameters affecting the effective exposure times and camera efficiency. The observational cost of this effort was about 40 shifts. Additional observing time was spent to obtain high resolution observations of some of the WDs and sdOs under an accepted proposal by the participants in the VILSPA meeting.

## III. The Photometric Calibration of the *IUE* Final Archive

The most interesting proposal made at the 1990 *IUE* Calibration Meeting at Villafranca was to define a relative flux scale based on model atmosphere fluxes of a suitable sample of hot DA White Dwarf stars whose fluxes could be predicted with enough accuracy (Koester 1990). In other words, the models could be used to derive the shape (but not the flux zero point) of the sensitivity curves of the *IUE* cameras. The DA White Dwarf G191 B2B was considered as the most suitable candidate as primary standard. A pure Hydrogen model with $T_{eff}$ = 58000 K and $g$ = 7.5, here adopted, was considered accurate enough for G191 B2B, with the estimated error in the effective temperature (between 1000 and 2000 K) small enough to introduce a maximum uncertainty in relative fluxes of about 2 percent over the *IUE* spectral range (Koester 1990). An additional advantage of G191 B2B is that, because of its high effective temperature and the consequently narrow Lyman profile, also the region near the short wavelength end of the SWP camera can be calibrated accurately. Although some authors have reported the presence of metals in the atmosphere of G191 B2B (see for instance Bruhweiler and Kondo 1981, Vennes 1992 or Barstow et al. 1993), their abundance is extremely low, so that the difference between pure Hydrogen models and models including metals is nearly negligible in the spectral range of interest (Finley, this volume).

The above-mentioned model of G191 B2B, together with several low resolution spectra of G191 B2B obtained in 1990–1991 were used to derive the relative inverse sensitivity curves of the SWP and LWP cameras in that period. The relative inverse sensitivity curves were then used to find the relative fluxes of the remaining standards, including other WDs, some sdO stars and the best classical standards, whose spectra were also obtained in 1990–1991.

The next step was to find a coherent way of defining the zero point of the absolute scale. A direct use of the model atmosphere absolute fluxes was excluded *a priori* because of the too large errors implied by the not yet adequate knowledge of the stellar parameters. A second possibility, also excluded, was to normalize the model fluxes to existing photometric or spectrophotometric observations in the optical range. The extrapolation of the fluxes over such a wide spectral range, from the optical to the UV, had, in fact, the major drawback of amplifying in the UV the uncertainty not only in the model, but also in the optical data. The choice finally made was to set the zero point by comparing, for the same star, the relative fluxes derived as described above, with the UV fluxes as measured by other space experiments. Which experiment to select as reference and in which wavelength the zero point should be set is of course the most critical problem. Finally, it was considered that the procedure ensuring the best accuracy was to find the flux zero point by scaling the relative fluxes of the brightest *IUE* classical standard stars taking as reference the *OAO-2* fluxes in the spectral band 2100–2300Å. Indeed, it is in this band where the previous space experiments agree best (within 2 percent for *OAO-2* and *TD1*, see Bohlin et al. 1980).

The absolute fluxes of the *IUE* standards observed in 1990–1991 were then used as input fluxes to derive the inverse sensitivity curves for 1985, chosen as zero epoch for the flux calibration of the *IUE* Final Archive output data. The corrections for time-dependent sensitivity degradation of the *IUE* cameras, implemented in the Final Archive, are referred to this epoch. A full description of the method as applied to the SWP and LWP cameras has been given in Gonzalez-Riestra et al. (1992, 1993).

The differences between the new and the old flux scales can be appreciated in Figure 1 where we show the ratio of the new flux and the old one (as given by Bohlin and Holm 1984) for two of the *IUE* standard stars (HD 60753 and $\lambda$ Lep). The discontinuities in this ratio clearly indicate the errors in the previous flux scale. Especially in the short wavelength range, there are large fluctuations of up to 15–20 percent over intervals less than 100Å wide. In the long wavelength range the ratio is more constant except for a substantial decrease longward 3100Å where the old fluxes were overestimated by 20 percent. Figure 2 shows the average ratios (New Flux/Old

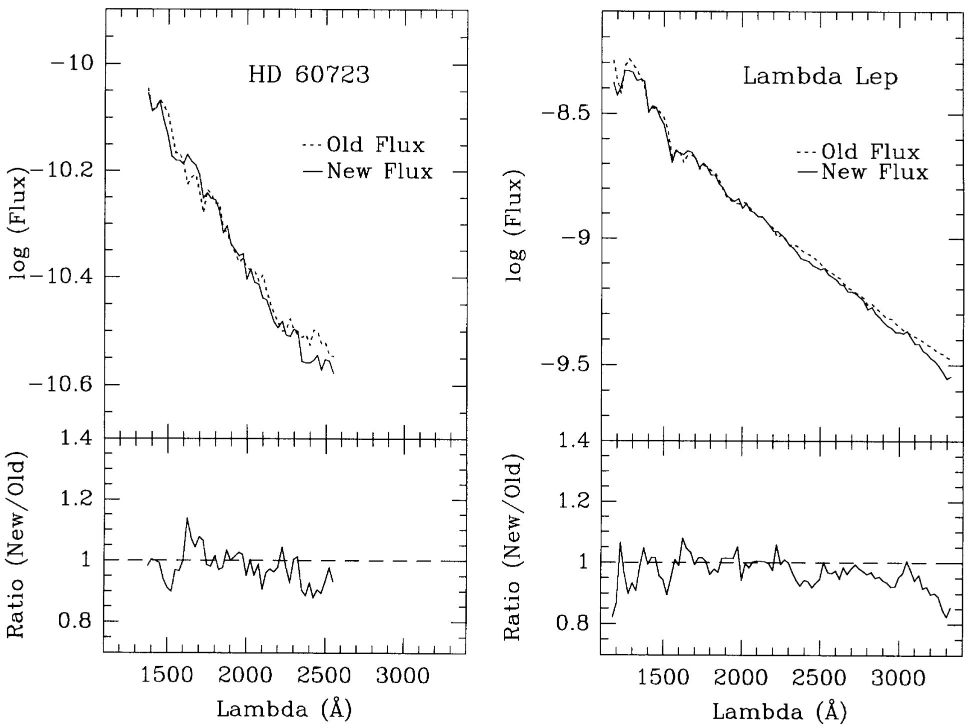


Figure 1: Comparison of old and new fluxes for the standard stars HD 60753 and Lep. The old fluxes have been taken from Bohlin and Holm (1984) and the new ones have been derived with the present calibration.

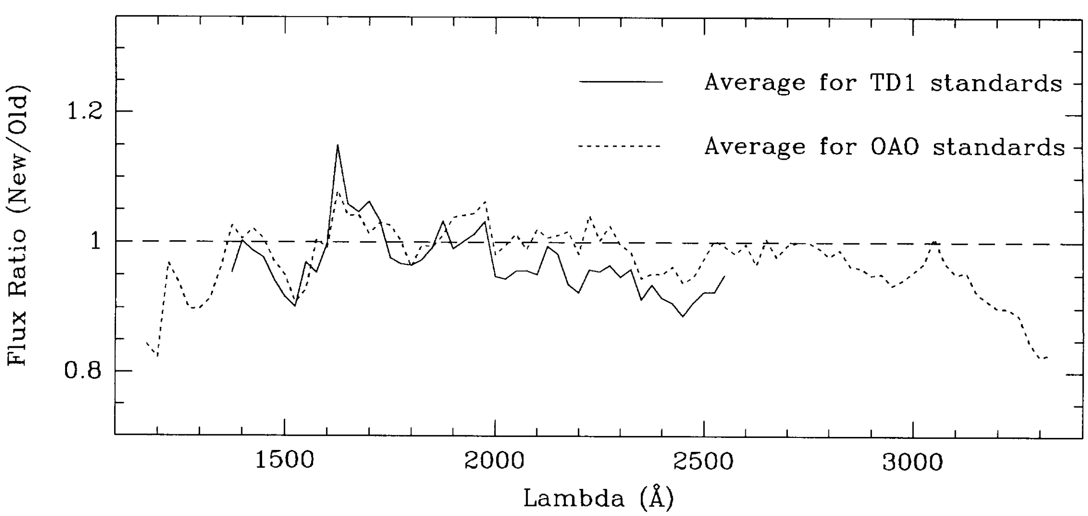


Figure 2: A verage ratios New flux / Old flux for *TD1* and *OAO-2* standards.

Flux) for several *TD1* and *OAO-2* standard stars. The factors to be used to put the original *TD1* and *OAO-2* fluxes in the new *IUE* Flux scale are shown in Figure 3, where they are compared to the correction factors given by Bohlin and Holm (1984).

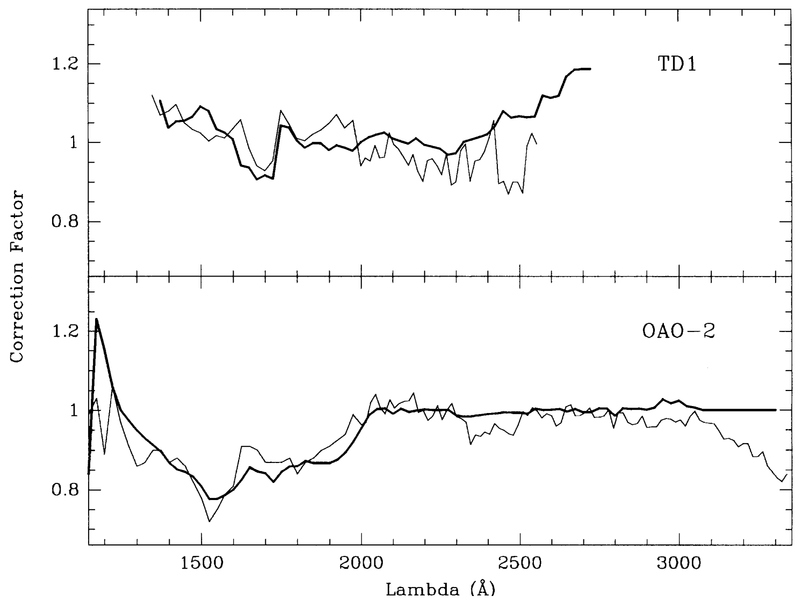


Figure 3: New correction factors to the original *TD1* and *OAO-2* fluxes (thin lines). For comparison, the correction factors given by Bohlin and Holm (1984) are shown as thick lines.

## References

Barstow , M.A., Fleming, T .A., Finley , D.S., Koester , D., Diamond, C.J. (1993) MNRAS 260, 631

Bohlin, R.C., Holm, A.V ., Savage, B.D., Snijders, M.A.J., Sparks, W .M. (1980) AA 85, 1

Bohlin, R.C. and Holm, A.V . (1984) *IUE* NASA Newsletter 24, p.74

Bruhweiler , F.C. and Kondo, Y . (1981) ApJ 248, L123

Cassatella, A. (1990) Report to the Three Agency Meeting, May 1990

Cassatella, A., Gonzalez-Riestra, R., Imhoff, C., Oliversen, N., Lloyd, C. (1992) AA 256, 309

Finley , D., Basri, G. and Bowyer , S. (1990) ApJ 359, 483

Greenstein, J.L. and Oke, J.B. (1979) ApJ 229, L141

Gonzalez-Riestra, R., Cassatella, A. and de la Fuente, A. (1992) Report to the Three Agency Meeting, November 1992

Gonzalez-Riestra, R., Cassatella, A. and de la Fuente, A. (1993) Report to the Three Agency Meeting, November 1993

Hackney , R.L., Hackney , K.R. and Kondo, Y . (1982) in "Advances in Ultraviolet Astronomy: Four years of *IUE* Research", ed. Y . Kondo, J.M. Mead and R.D. Chapman, NASA CP-2238, p. 335

Koester , D. (1990) Report to the *IUE* Calibration Meeting, VILSP A

Nichols-Bohlin, J., de la Pena, M., Linsky , J., Kondo, Y ., Michalitsianos, A., Ponz, J.D., T alavera, A., Gonzalez-Riestra, R., W amsteker , W. (1993) in "Frontiers of Space Science and Ground-based Astronomy", in press

Vennes, S. (1992) ApJ 390, 590

# Calibration of the Hopkins Ultraviolet Telescope

Jeffrey W. Kruk [1]

## Abstract

The Hopkins Ultraviolet Telescope (*HUT*) flew aboard the space shuttle Columbia during the Astro-1 mission in December, 1990. *HUT* has been optimized for obtaining spectrophotometric observations of faint objects at wavelengths ranging from the Lyman limit (912Å) up to 1860Å. The telescope layout is shown in Figure 1, and the instrument parameters are given in Table 1. Calibrations were performed pre-flight, in-flight, and post-flight. These calibrations are described below.

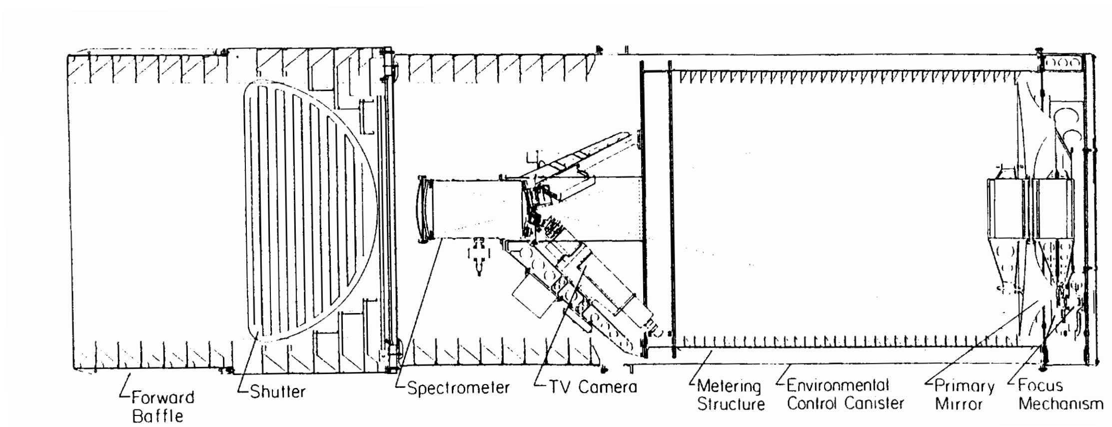


Figure 1: *HUT* layout

## I. Pre-Flight Calibration

The pre-flight calibration consisted of separate measurements of the reflectivity of the primary mirror and spectrograph throughput, since the large size of the telescope precluded a laboratory calibration of the instrument as a whole. The primary mirror reflectivity was determined at 8 wavelengths at numerous points over its surface, by comparing its reflectivity at each point with that of an iridium coated test flat whose reflectivity was measured in a conventional reflectometer. The primary mirror reflectivity was subsequently monitored with iridium coated witness mirrors which accompanied the primary mirror at all times. The spectrograph throughput was measured at 29 wavelengths and at 19 entrance angles distributed over the f/2 cone of the telescope. The incident fluxes were determined using both a microcline plate detector and an EMR G tube which were calibrated against photodiodes which in turn were calibrated at NIST. The resulting pre-flight determination of the effective area for first order wavelengths is shown in Figure 2a.

---

1. CAS, Johns Hopkins University, Baltimore, MD 21218

**Table 1: *HUT* Instrument Characteristics**

| | |
|---|---|
| Telescope | |
| Prime Focus Paraboloid | |
| Aperture | 0.9 m |
| Focal Ratio | f/2 |
| Plate scale | 8.727 microns/arc sec |
| Mirror Coating | Iridium |
| Aperture Door Areas | 5120, 2560, 50, 1 cm**2 |
| Spectrograph | |
| Rowland Circle Mounting | |
| Grating Diameter | 200 mm |
| Radius of Curvature | 400 mm |
| Grooves | 600 l/mm, holographic |
| Coating | Osmium |
| Spectral Resolution | 3Å |
| Wavelength Coverage | 830–1860Å, 415–930Å |
| Scattering | $1x10^{-5}$ per Å |
| Detector | |
| Open Window Microchannel Plate Intensifier | |
| Photocathode | Cesium Iodide |
| MCP's | two 80:1 L/D, 10 pores, 15 degree bias |
| Anode | Phosphor screen with photodiode readout |
| Active Length | 25 mm |
| Diode Size | 25 µm x 2.5 mm |
| Time Resolution | 1 msec |
| Background | $7.7x10^{-4}$ counts/sec/Å |
| Electron Repeller Grid | 95 percent Transmission, 20 l/inch |

A mercury lamp mounted on the spectrograph provided a rough monitor of the throughput over the two years prior to the flight. The observed count rate from the lamp declined steadily by about 25 percent over this period, and both in-flight and post-flight calibrations give a throughput 20-30 percent below the pre-flight calibration. The observed rate from the lamp has been stable since the flight, indicating that the post-flight calibration should be representative of the actual in-flight sensitivity . These results are consistent with our experience for CsI photocathode aging. The ratio of the post-flight to preflight calibrations is shown in Figure 2b.

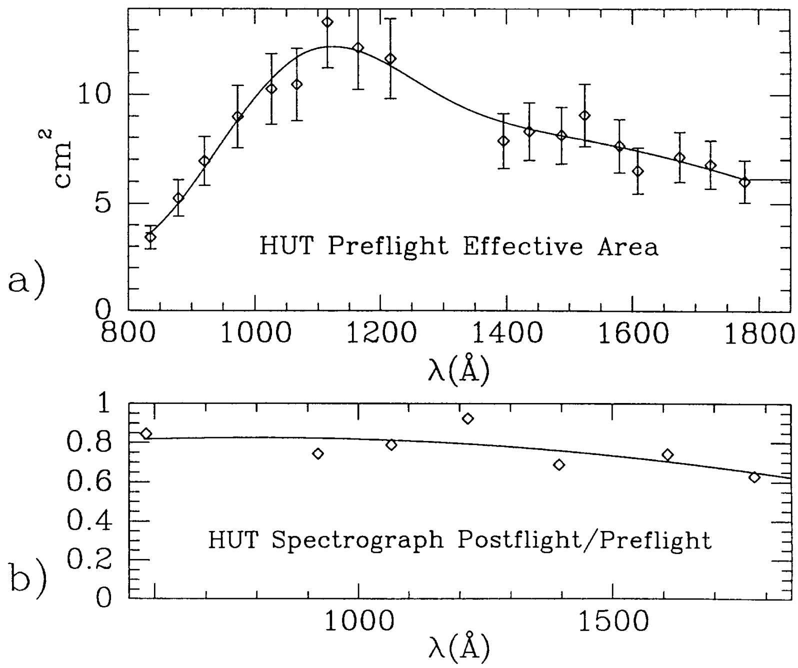


Figure 2: a) preflight calibration; b) ratio of post/pre flight calibrations.

## II. In-Flight Calibration

Our first order flux calibration is defined by the model atmosphere for the DA white dwarf G191-B2B of P . Bergeron. The model parameters $T_{eff}$ = 59,250 K and log $g$ = 7.5 were determined from observations at visual wavelengths (Holberg et al., 1991).

The raw spectrum is corrected for phosphor persistence (7.3 percent), detector dark count (0.01–0.1 percent), detector deadtime (5 percent at peak of spectrum), and second and third order flux ( $\leq$ 3 percent). The model itself is corrected for transmission through the interstellar medium ($N_H$ = 1.7x10$^{18}$ cm$^{-2}$, b = 10 km/s). Uncertainties in the proper effective temperature lead to changes in our effective area of less than 5 percent, to within a few angstroms of the L yman edge. The resulting flux-calibrated spectrum and the model spectrum are shown in Figure 3. The apparent absorption feature at 1600Å is a detector defect and the peak at 1216Å is contamination from airglow . Other small deviations of the spectrum from the model are due to the requirement that our effective area curve vary smoothly with wavelength.

A test of the model dependence of the calibration can be made by comparison with a different model atmosphere. Our adopted flux for G191-B2B and the model atmosphere of D. Coaster are shown in Figure 4, for 900–1 140Å (the two models give essentially identical results longward of 1 100Å). The only appreciable differences between the models occur between the strong L yman β, γ, and δ absorption lines, due to differences in the treatment of pressure broadening.

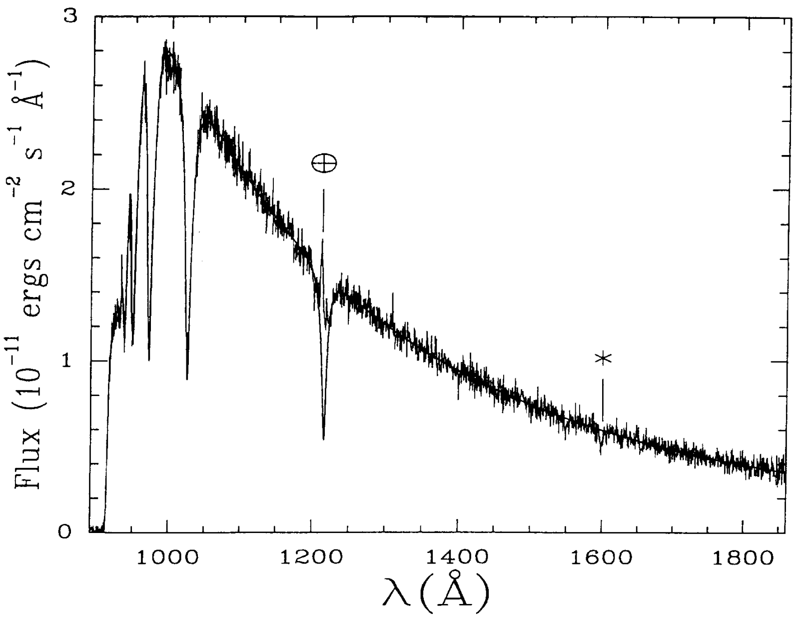


Figure 3: Comparison of HUT spectrum of G191-B2B with model from P . Bergeron.

An additional test of the calibration is provided by comparing the observed spectrum of the white dwarf HZ43 with the Koester model for this star . All parameters in this model were determined by observations made at visual wavelengths. The *HUT* spectrum has been multiplied by 1.08 to account for pointing jitter . The *HUT* spectrum and the model are shown in Figure 5. The peaks seen at 1216 and 1304Å are due to airglow . No systematic disagreements greater than a few percent are seen longward of about 975Å. Shortward of 975Å the data falls as much as 15 percent below the model, which may reflect slight errors in the adopted temperatures of HZ 43 or G191-B2B, or may be due to differences in modelling absorption by the converging L yman series in the presence of severe pressure broadening.

Calibrations for the various aperture door configurations were obtained by observing suitable stars through multiple doors.

## III. Post-Flight Calibration

The post-flight calibration of the spectrograph was performed one year after the mission. W e repeated the pre-flight spectrograph calibration at a subset of wavelengths and angles, and multiplied by the pre-flight mirror calibration to obtain the effective area. The results are shown in Figure 6, along with the in-flight effective area calibration. While fluctuations of up to 10 percent are seen, the mean ratio differs from unity by less than 1 percent. This agreement is fortuitously good, given that the uncertainties in the calibration of the NIST photodiodes used in the laboratory measurements are greater than this.

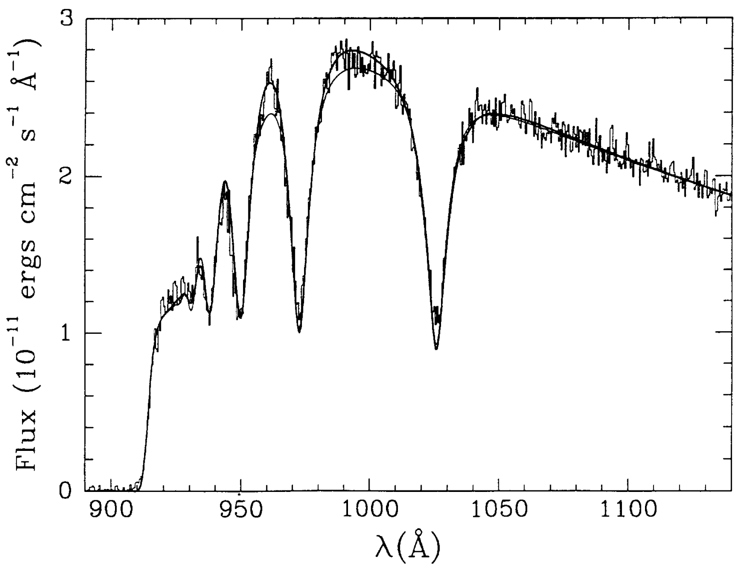


Figure 4: Comparison of adopted flux for G191-B2B with model from D. Coaster .

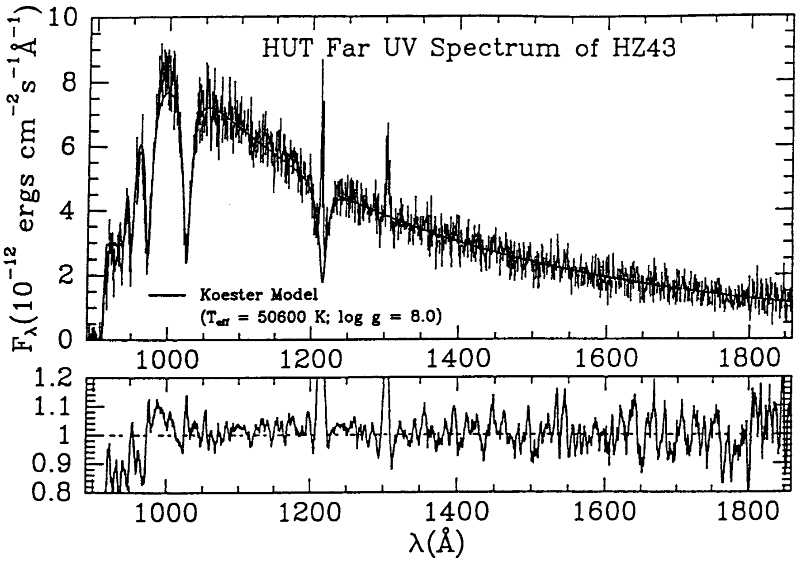


Figure 5: Comparison of *HUT* spectrum of HZ43 with model from Koester .

We recently gained access to the primary mirror and measured its reflectivity at 1236Å. It is unchanged from its pre-flight value of 19 percent. A more detailed measurement of the mirror reflectivity will be performed when it is shipped back to JHU.

We also performed a post-flight spectrograph calibration at SURF . There were two aspects to this calibration: determining the detector response to a flat field, and determining the absolute spectrograph efficiency .

The flat field measurements revealed two types of features: shadows cast by the wires of the electron repeller grid, and a defect in the detector in the vicinity of pixel 1510 (corresponding to 1600Å in the first order spectrum). The dip at about pixel 760 is caused by reduced gain in the microchannel plates where they were illuminated by the intense geocoronal L yman alpha radiation. A typical spectrum obtained at a single entrance angle is shown in Figure 7.

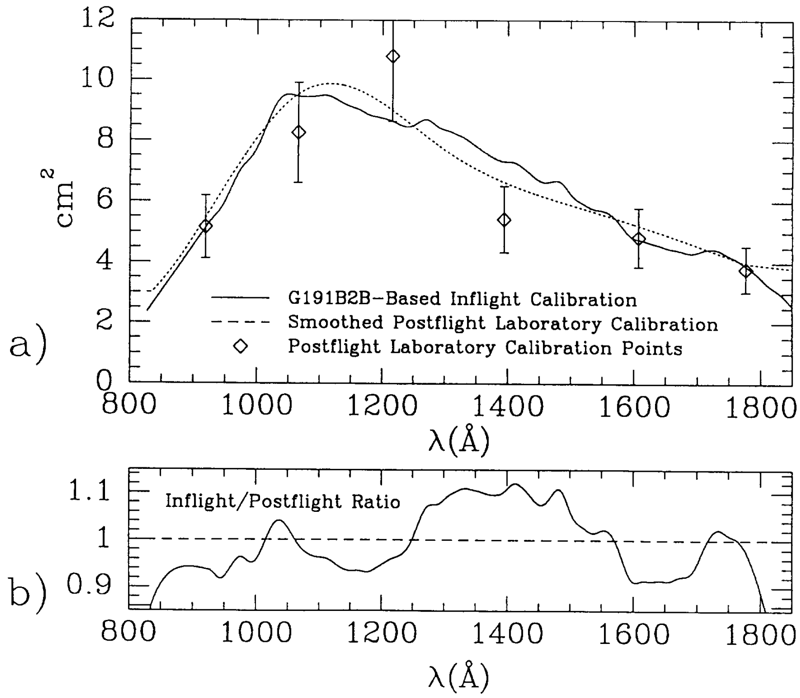


Figure 6: Comparisons of in-flight and post flight calibrations.

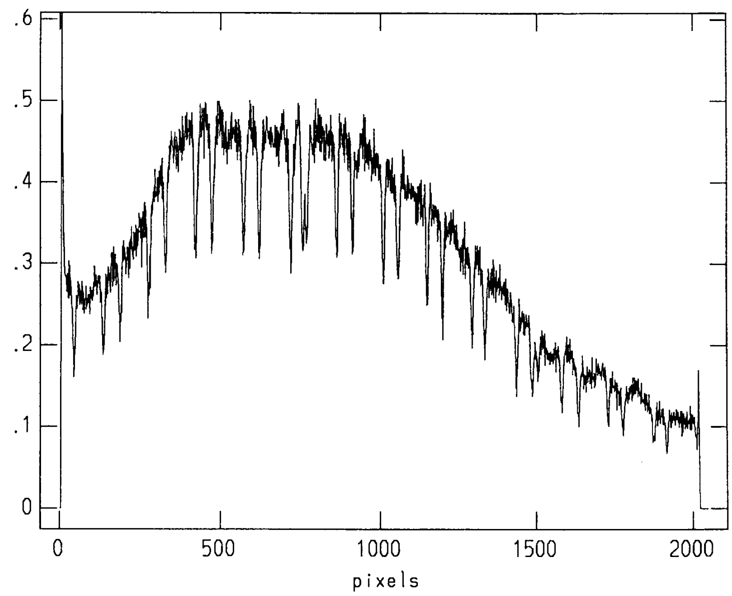


Figure 7: Flat field taken at a single entrance angle, note the effect of the wires of the electron repeller guide on the flat field.

The wire shadows are effectively smoothed out by the f/2 beam obtained for observations made through the large telescope doors, but not by the f/20 beam produced by the 50 cm$^2$ door. A correction for this effect was determined by measuring the spectrograph response at 26 entrance angles distributed evenly over this f/20 cone. The resulting average is shown in Figure 8. A smooth curve was fit to the dips in this average spectrum to serve as a flat field correction for all observations made through the 50 cm$^2$ door. This correction was tested by coadding spectra of three hot stars observed by both *HUT* and *IUE*, and comparing the ratio of the *HUT*

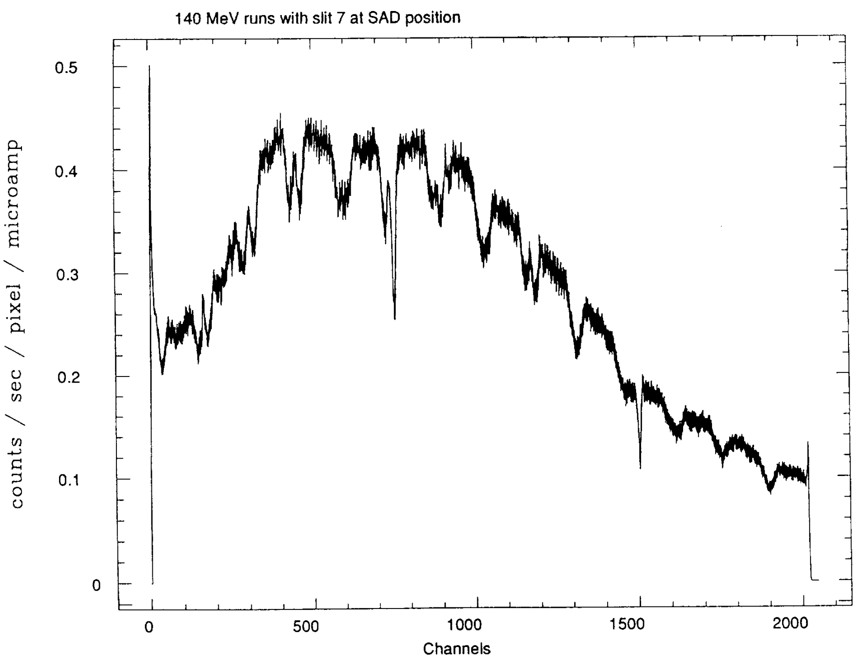


Figure 8: A verage flat field as described in text.

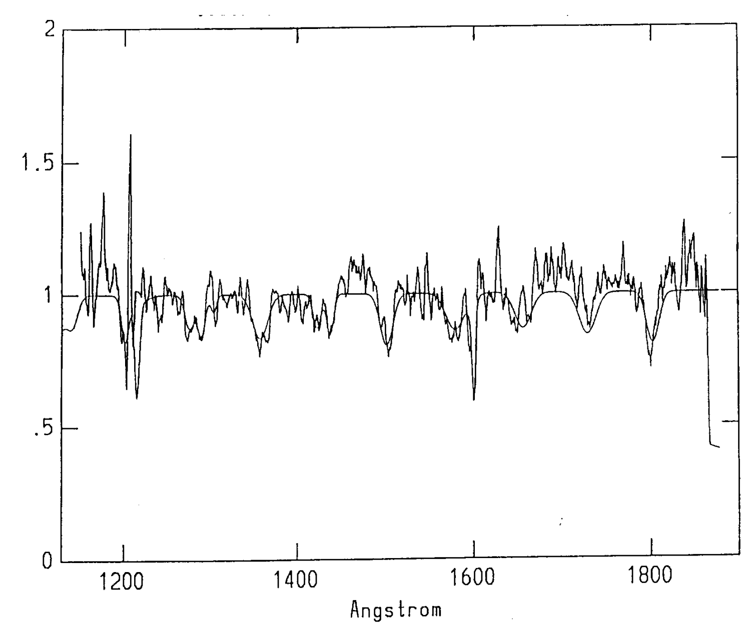


Figure 9: Comparison of the ratio of *HUT* to *IUE* observations with proposed correction for flat field features.

to *IUE* spectra with the proposed correction. The agreement is quite good, as can be seen in Figure 9.

The efficiency calibration was complicated by the fact that the spectrograph has measurable sensitivity through the first 4 diffraction orders. At the normal SURF beam energy of 284 MeV the flux rises with decreasing wavelength about as fast as our grating efficiency falls, with the result that the observed count rates were comparable in all four orders. In normal operation the flux is cut off at 912Å by the interstellar medium, but no such filter is available at SURF! Attempts to run at four different beam energies and solve directly for the spectrograph efficiency in the first four grating orders were not successful. However, data taken at a beam energy of 100 MeV had sufficiently little flux in our higher order bandpass (2-3 percent of first order) to be easily modelled and subtracted. Since the synchrotron had never been run at 100 MeV, the potential systematic errors are difficult to assess. We attempted to account for these by obtaining a second calibration at the usual beam energy of 284 MeV through cross-calibrated magnesium fluoride and calcium fluoride filters. This produced a calibration useful longward of 1260Å, which was used to fix the beam energy and orbital plane tilt of the 100 MeV data. Due to limitations in available beam time we only took such data at the center of the grating. We multiplied these data by a smooth fit to the ratio of grating average to grating center sensitivity obtained at fixed wavelengths in the JHU calibration facility. This result is shown in Figure 10, along with the in-flight determination of the spectrograph efficiency (calculated by dividing the in-flight effective area curve by the pre-flight measurements of the primary mirror effective area). These two calculations generally agree to within a few percent, with occasional disagreements of up to 7 percent. The discrepancy does grow below the Lyman edge, (to about 20 percent at 830Å, where we have no in-flight calibration data. The sharp peaks seen at either end of the spectrum are due to mis-centroided events at the edge of the detector active area. The ripples seen in the SURF data are due to the fact that the long slit used in the measurement shown does not smooth out the shadows cast by the repeller grid as effectively as the f/2 beam of the full telescope.

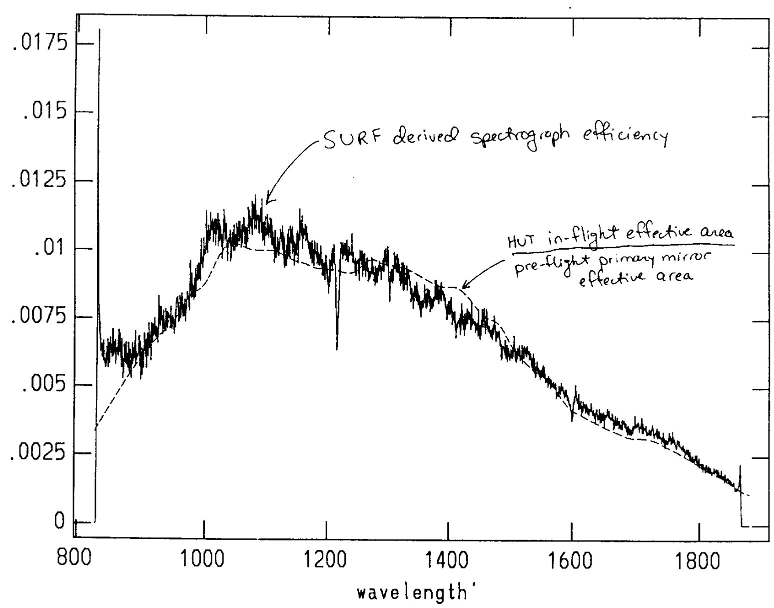


Figure 10: SURF calibration

## IV. Comparison with Other Instruments

Figure 11 shows spectra of G191-B2B from *HUT*, *IUE*, and Voyager. The agreement is quite good, apart from broad undulations in the *IUE* spectrum of up to 10 percent. These undulations are inherent in the old *IUE* calibration used in this plot; they

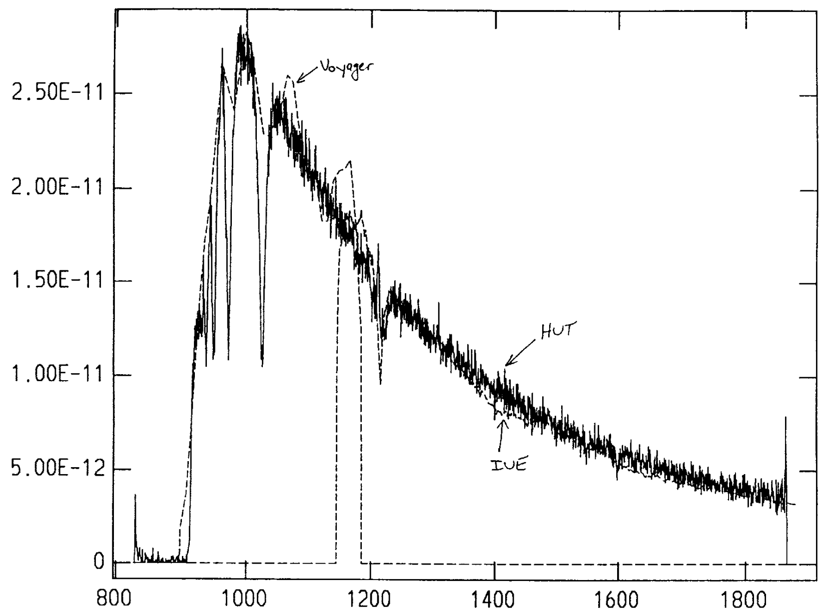


Figure 1 1: Spectra of G191-B2B from *HUT* , *IUE* and V oyager .

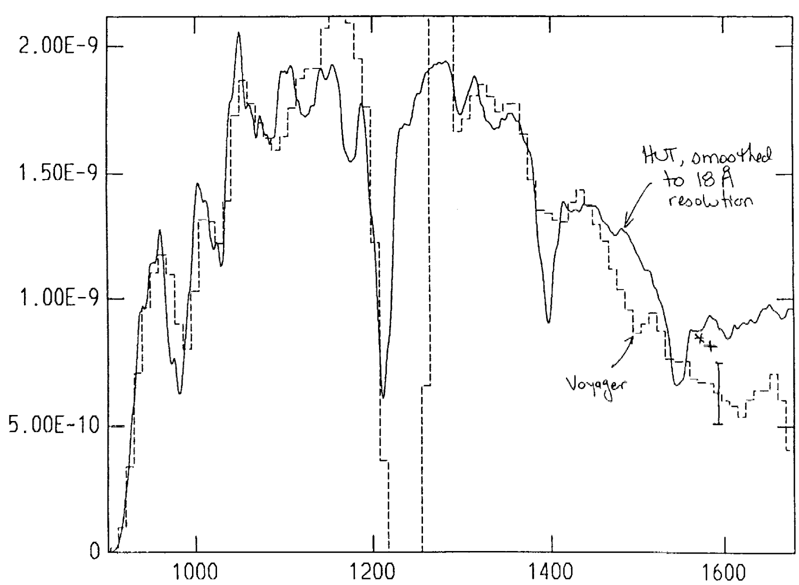


Figure 12: Spectra of π Agr from V oyager and *HUT* .

would disappear if the new *IUE* calibration had been used. Figure 12 shows spectra of πAqr from V oyager , and from *HUT* (after smoothing to match the V oyager resolution). The agreement is again excellent.

## V. Conclusion

The absolute first order sensitivity of *HUT* , as defined by the model atmosphere for G191-B2B, is in agreement with post-flight laboratory calibrations to within the 10 percent uncertainty of the laboratory data. Different atmosphere models disagree, typically by about 5 percent, for wavelengths below 1000Å. This is due in part to the extreme sensitivity of the flux at these wavelengths to small changes in the effective temperature, and in part to difficulties in modelling line broadening effects in the vicinity of the converging Lyman series. The Astro-2 guest investigator program of Dave Finley will address this problem. The *HUT* laboratory calibration should help resolve the controversies that have existed shortward of Lyman $\alpha$, where various instruments have disagreed by factors of as much as 4 to 6 (Holberg et al. 1991, and references therein). Several refinements of our calibration procedures are planned for the Astro-2 mission, which should enable us to improve upon the accuracy obtained for Astro-1.

**References**

Holberg et al., ApJ 375, 716 1991.

# Precision Photometry at the LMC Centre: Simulating Post-COSTAR *HST* Observations

P. Linde [1], R. Snel [1] and S. Spannare [1]

## Abstract

We intend to use the restored *HST* to study age structure and chemical evolution of the stellar population at the centre of the LMC. To obtain the necessary observational parameters, Strömgren photometry is planned using the Planetary Camera. To study the reduction techniques needed, a set of simulated PC images have been made. These images are based on extrapolated luminosity functions and show a high degree of crowding. Two of the generally available photometric software packages, Romafot and DAOphot, have been used to analyze the images. Results show that the photometric accuracy reached with these packages is not enough for high precision photometry in this configuration. We show that the two major contributors to the errors are under-sampling and the unusual shape of the point spread function. Adaptation of locally developed software is currently in progress to deal with these problems.

The full paper appears in the companion volume, The Restoration of *HST* Images and Spectra, vol. 2.

1. Lund Observatory, Box 43, S-221 00, Lund, Sweden